PHYSICAL REVIEW B **94**, 085202 (2016)

Tunability of the dielectric function of heavily doped germanium thin films for mid-infrared plasmonics

Jacopo Frigerio, Andrea Ballabio, and Giovanni Isella
L-NESS, Dipartimento di Fisica, Politecnico di Milano, Polo di Como, Via Anzani 42, I-22100 Como, Italy

Emilie Sakat, Giovanni Pellegrini, and Paolo Biagioni
Dipartimento di Fisica, Politecnico di Milano, Piazza Leonardo da Vinci 30, I-20100 Milan, Italy

Monica Bollani
CNR-IFN and L-NESS, Via Anzani 42, I-22100 Como, Italy

Enrico Napolitani
Dipartimento di Fisica e Astronomia, Universitá di Padova and CNR-IMM MATIS, Via Marzolo 8, I-35131 Padova, Italy

Costanza Manganelli
Scuola Superiore SantAnna, via G. Moruzzi 1, I-56124 Pisa, Italy

Michele Virgilio
Dipartimento di Fisica "E. Fermi", Universitá di Pisa, Largo Pontecorvo 3, I-56127 Pisa, Italy

Alexander Grupp, Marco P. Fischer, and Daniele Brida
Department of Physics and Center for Applied Photonics, University of Konstanz, D-78457 Konstanz, Germany

Kevin Gallacher and Douglas J. Paul
School of Engineering, University of Glasgow, Rankine Building, Oakfield Avenue, Glasgow G12 8LT, United Kingdom

Leonetta Baldassarre, Paolo Calvani, Valeria Giliberti, Alessandro Nucara, and Michele Ortolani*
Dipartimento di Fisica, Sapienza Universitá di Roma, Piazzale Aldo Moro 5, I-00185 Rome, Italy

(Received 16 May 2016; revised manuscript received 27 July 2016; published 15 August 2016)

Heavily doped semiconductor thin films are very promising for application in mid-infrared plasmonic devices because the real part of their dielectric function is negative and broadly tunable in the 5 to 50 μm wavelength range at least. In this work, we investigate the electrodynamics of heavily n-type-doped germanium epilayers at infrared frequencies beyond the assumptions of the Drude model. The films are grown on silicon and germanium substrates, are *in situ* doped with phosphorous in the 10^{17} to 10^{19} cm^{-3} range, then screened plasma frequencies in the 100 to 1200 cm^{-1} range were observed. We employ infrared spectroscopy, pump-probe spectroscopy, and dc transport measurements to determine the tunability of the plasma frequency. Although no plasmonic structures have been realized in this work, we derive estimates of the decay time of mid-infrared plasmons and of their figures of merit for field confinement and for surface plasmon propagation. The average electron scattering rate increases almost linearly with excitation frequency, in agreement with quantum calculations based on a model of the ellipsoidal Fermi surface at the conduction band minimum of germanium accounting for electron scattering with optical phonons and charged impurities. Instead, we found weak dependence of plasmon losses on neutral impurity density. In films where a transient plasma was generated by optical pumping, we found significant dependence of the energy relaxation times in the few-picosecond range on the static doping level of the film, confirming the key but indirect role played by charged impurities in energy relaxation. Our results indicate that underdamped mid-infrared plasma oscillations are attained in n-type-doped germanium at room temperature.

DOI: 10.1103/PhysRevB.94.085202

The recent push towards applications of spectroscopy for chemical and biological sensing in the mid-infrared (mid-IR) [1–8] has prompted the search for conducting thin films displaying values of the complex dielectric function $\tilde{\epsilon}(\omega) = \epsilon'(\omega) + i\epsilon''(\omega)$ that can be tailored to meet the needs of novel electromagnetic designs. These exploit the concepts of metamaterials, transformation optics, and plasmonics [9]. For example, in the design of metamaterials, subwavelength-sized conducting elements are embedded in dielectric matrices. If the values of $|\epsilon'|$ of the metal and the dielectric are of the same order, but have opposite sign, the geometric filling fractions of the metal and dielectric can be readily tuned to achieve subwavelength-resolution focusing of radiation [10]. Such requirement is, e.g., met by Au in the green part and Ag in the blue part of the visible spectrum. The same condition

*michele.ortolani@roma1.infn.it

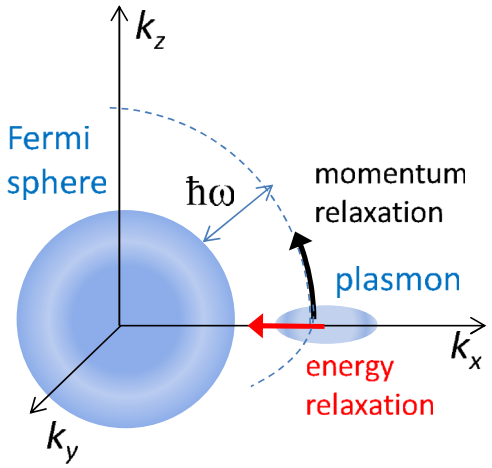

FIG. 1. A schematic view in the k space of a classical plasmon of frequency ω propagating along the x direction, in the case of an isotropic three-dimensional electron liquid. The blue areas represent occupied electron states. Two types of decay channels exist for the plasmon: momentum relaxation by elastic scattering of electrons (black arrow) and energy relaxation by inelastic scattering (red arrow). Many electron scattering events of the two types may be needed for complete plasmon decay.

cannot be achieved in the far-IR or mid-IR range by using elemental metals, however, because they possess an extremely high negative value of ϵ' not equaled, in absolute value on the positive side, by any dielectric material. It has been proposed that, in order to obtain tunable values of ϵ' in the entire IR range [11,12], heavily doped semiconductors [13–19] and conducting oxides [20] may be used because their free-carrier density can be set by selecting the doping level and further tuned by electrostatic gating [16] or optical excitation [21,22].

Beyond dielectric function tunability, a key requirement in plasmonics and metamaterial design is a low level of intrinsic losses in the material. Specific effects such as nanofocusing, field confinement, or phase front shaping are obtained by creating subwavelength geometrical structures to engineer the propagation of a specific mode of the electromagnetic field. Any physical process, which leads to modification of the electron energy and/or momentum distribution corresponding to the specifically engineered electromagnetic field mode, contributes to plasmon losses (see scheme in Fig. 1). For a given material, it is possible to make an assessment on the average single-electron scattering rate, which is an intrinsic property, but not on the plasmon decay time, which may be also dependent on the specific device layout, the dielectric environment, the surface roughness, and/or the finite size of the subwavelength elements. At IR frequencies, intrinsic losses are represented by nonradiative decay of interband transitions and intraband free-carrier excitations. Excluding perhaps superconductors, which can be used only in the microwave and terahertz ranges [23–25], low intrinsic losses are hard to achieve in all classes of materials that have been considered for plasmonics and metamaterial applications. Interband transitions can be avoided only in material-specific frequency ranges; metal films deposited by standard techniques such as evaporation or sputtering display polycrystalline structures that increase finite-size and surface roughness effects; conducting oxides are characterized by high crystal defect densities [20]; compound semiconductors have strong dipole-active optical phonons that both directly absorb IR radiation and efficiently scatter the conduction electrons; finally, doped materials in general present charged-impurity densities that increase proportionally to the doping level and produce Coulomb scattering of free carriers. Energy transfer from the collective electromagnetic field mode to the incoherent motion of individual electrons and polar phonons in the material is quantified by $\epsilon''(\omega) > 0$, which can therefore be taken as a figure of merit for intrinsic losses. It is worth noting that the only materials showing a wide range of negative values of $\epsilon'(\omega)$ together with almost vanishing $\epsilon''(\omega)$ are surface-phonon-polariton materials, like silicon carbide [26] and boron nitride [27], where the negative value of $\epsilon'(\omega)$ is not due to free carriers but to IR-active phonons. These materials, however, can operate in a very narrow and nontunable range between the end of the transverse optical phonon absorption tail and the longitudinal optical phonon frequency, which is ultimately defined by the crystal structure and is therefore characterized by a very limited tunability of the associated surface-phonon-polariton resonances [28].

The ensemble of these considerations has led us to propose heavily doped Ge thin films and to study their electrodynamic properties in the mid-IR range, here defined as the wavelength range 20 μm $> \lambda >$ 5 μm, or the electromagnetic frequency range 500 cm^{-1} $< \omega <$ 2000 cm^{-1}, or the photon energy range 60 meV $< \hbar\omega <$ 250 meV. The lack of polar phonons and therefore the weak electron-phonon interaction if compared to most compound materials provides one with the opportunity to evaluate the effect of charged-impurity scattering on mid-IR plasmon decay. Moreover, epitaxial germanium films can be grown by chemical vapor deposition (CVD) on both ideal lattice-matched bulk Ge wafers and lattice-mismatched silicon wafers, hence allowing one for the study of effect of crystal defect density on the plasmon decay. Also, this fact represents a further advantage of germanium for applications in mid-IR plasmonics because silicon substrates are compatible with the mainstream silicon microfabrication technology process.

The high-frequency limit for conducting behavior of a given material with free-carrier density n and effective mass m^* is ultimately set by the *screened plasma frequency* ω^* where $\epsilon'(\omega^*) = 0$, being negative for $\omega < \omega^*$, approximately given (in the limit of low losses) by

$$\omega^* \simeq \sqrt{\frac{4\pi n e^2}{\epsilon_\infty m^*}}. \quad (1)$$

Gaussian units are used throughout the paper where e is the free-carrier charge and ϵ_∞ is the high-frequency dielectric screening constant, which can be thought of as the mid-IR permittivity of the corresponding undoped material. For germanium, $\epsilon_\infty \simeq 16$. In a three-dimensional conductor, ω^* approximately scales with the free-carrier density n as $\sqrt{n}$, which then becomes the main optimization parameter for electromagnetic design. This work is devoted to the study of the optical properties of electron-doped germanium (n-Ge) thin films relevant for mid-IR plasmonics. These properties include n spanning two orders of magnitude, small m^* and

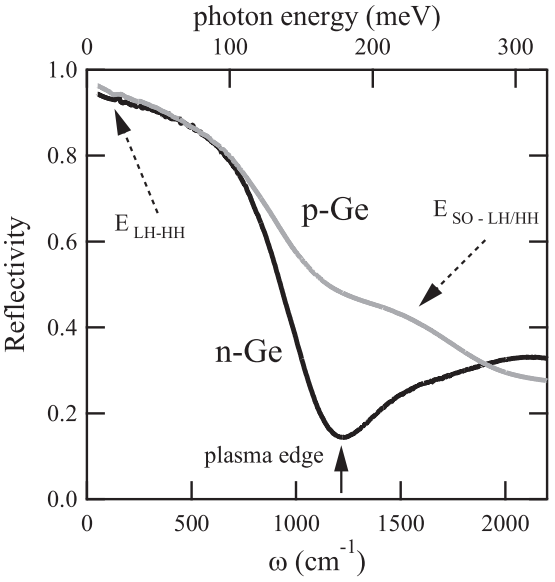

FIG. 2. Reflectivity of two Ge films grown on Si wafers. One film was hole doped (p-Ge) and one electron doped (n-Ge). The thickness is 1 μm and the free-carrier density is 2×10^{19} cm^{-3} for electrons and 7×10^{19} cm^{-3} for holes. The plasma edge is evident only in the n-Ge film (continuous arrow). The energy of the transition between different valence bands impacting on the intrinsic plasmon losses of p-Ge is indicated by dashed arrows.

thus ω^* reaching values well into the mid-IR. We present the experimental determination of the IR dielectric function of Ge thin films grown by CVD on different substrates. We demonstrate that this material displays both wide tunability of $\epsilon'(\omega)$ and values of $\epsilon''(\omega)$ limited only by the fundamental quantum processes of electron-phonon and electron-charged-impurity scattering. In order to quantify the role of the different loss mechanisms, we have developed a quantum model of electron scattering rates for different values of the doping level and we have conducted time-resolved pump-probe experiments to estimate its characteristic energy relaxation time. Although the quantitative results of this paper specifically apply to n-Ge, the method for plasmon loss determination can be applied to other doped materials.

Germanium is a close-to-ideal material for mid-IR optics. The main impurity-state transitions lie in the far-IR range, therefore, lightly doped films display almost no absorption in the entire mid-IR range and a frequency-independent value of the refractive index $\eta = 4.0$. The fundamental energy gap is indirect and equal to $E_g = 0.66$ eV, while the first direct interband transition edge is at $E_0 = 0.80$ eV, and this leads to an increase of the optical absorption above $\sim$6000 cm^{-1}, i.e., well above the mid-IR range of interest for molecular sensing. These features result in the abrupt decrease of the normal-incidence mid-IR reflectivity of n-Ge films from a value close to 1 at low frequencies to an absolute minimum just above ω^* (*plasma edge*, see Fig. 2) where $\epsilon' \sim 1$ and refractive-index matching with vacuum suppresses the reflected intensity. The conduction band minimum of Ge is at the L points of the electron wave-vector $\mathbf{k}$ space (intercept of the $\langle 111 \rangle$ axes with the first Brillouin zone) which leads to a Fermi surface (for n-doped materials) made of four ellipsoids with two short axes (corresponding to the small transverse effective mass $m_T = 0.0815m_e$) and one long axis (large longitudinal effective mass $m_L = 1.59m_e$). In the limit of vanishing momentum acquired by the electrons from the electric field, which is of interest for the isotropic optical and dc conductivities, the relevant quantity is the so-called *conductivity effective mass* $m^* = 0.12m_e$ calculated as described in Ref. [29]. Since ω^* scales with $1/\sqrt{m^*}$, the relatively low value of m^* makes n-Ge appealing for mid-IR plasmonic applications if compared to large-m^* materials such as electron-doped Si ($m^* = 0.26m_e$), Al-doped ZnO ($m^* = 0.29m_e$), or $In_{1-x}Ti_xO$ ($m^* = 0.35m_e$), and it compares well with electron-doped compound semiconductors such as GaAs ($m^* = 0.063m_e$) and InAs ($m^* = 0.023m_e$). Indeed, for a given value of the free-carrier density n (hence of the charged-impurity scattering losses), a higher ω^* is obtained when m^* is small.

One may recall that bands with small m^* can be found in hole-doped Ge (p-Ge) if compared to n-Ge [30]. The presence of multiple electronic bands in the energy range of the valence band of cubic semiconductors with the diamondlike structure (including Ge), however, implies the existence of interband transitions between the different valence bands in the entire IR range, not fully inhibited by the interband dipole selection rule and leading to plasmon losses. In particular, the transition between the light-hole (LH) and the heavy-hole (HH) band around the Γ point takes place in a broad frequency range in the far-IR (10 meV $< E_{\text{LH-HH}} <$ 100 meV) due to the different effective masses of the two hole types that make the two bands nonparallel in $\mathbf{k}$ space. The transitions from the split-off (SO) band to both the LH and HH bands is also activated by hole doping, is very broad, and sits at $E_{\text{SO-LH/HH}} \sim 289$ meV [31], exactly in the mid-IR range of technological interest. Instead, for n-Ge the only interband transition between different conduction bands is the diagonal L-to-Γ transition at $E \sim$ 140 meV, which requires a high momentum exchange with the lattice and has negligible optical spectral weight. These predictions are confirmed by the IR reflectivity of p-Ge thin films epitaxially grown on silicon wafers. In Fig. 2, the absolute reflectivity spectrum of p-Ge demonstrates a strong signature of the SO-LH/HH transitions between 150 and 250 meV (indicated by dotted arrow), to be contrasted with the plasma edge clearly observed in the reflectivity spectrum of n-Ge, which is indicative of a pure free-carrier response with neither interband nor impurity state transitions in the mid-IR. To summarize, intervalence band transitions in the entire IR range produce doping- and ω-dependent contributions to $\epsilon''(\omega)$ that would eventually undermine any design attempt for plasmonics in p-Ge. Dramatically, the strength of such lossy interband transitions increases with increasing hole doping because more final empty states become available. Instead, n-Ge displays all the *a priori* characteristics to perform as an ideal mid-IR plasmonic material. It remains to be determined how broadly the dielectric function of n-Ge can be tuned and how much the unavoidable free-carrier losses impact on mid-IR plasmon lifetimes. This is the subject of this paper.

The paper is organized as follows. In the first section, we demonstrate the high tunability of the n-Ge plasma frequency by selection of the doping level during thin-film growth. In the second section, we analyze the absolute reflectivity spectra in the entire far-to-near IR and we discuss

the limitations of the Drude-Lorentz model of the dielectric function based on a frequency-independent electron scattering rate. As an alternative method of loss evaluation, we calculate the dielectric function and the frequency-dependent electron scattering rate in a model-independent way exploiting the Kramers-Kronig relations. In the third section, we perform first-principles calculations of the electron scattering as a function of temperature, doping, and frequency, including the effect of phonons and charged impurities, and we use the model for interpretation of the transport and spectroscopy data and for identification of the main loss mechanisms of mid-IR plasmons. In the fourth section, we present a direct measurement of the collective energy-relaxation time in optically pumped n-Ge films, from which we derive a quantitative estimate of plasmon decay times in the mid-IR.

I. TUNABILITY OF FREE-CARRIER DENSITY IN THIN FILMS

Different dopants can be incorporated into the lattice sites of Ge, but since we employ silicon-foundry compatible CVD techniques requiring non-metal-organic gas precursors, the choice is limited to B for hole doping and P and As for electron doping. In this work, we will focus on films doped by phosphorous atoms since this is expected to give higher electron concentrations [32]. Indeed, Ge epilayers doped with P have displayed carrier densities exceeding 10^{20} cm^{-3} [33,34]. From here on, the word *doping* indicates the free-electron concentration n. We will analyze the effect of the incorporation of P atoms in the Ge lattice on n and on the electron scattering rate, leaving the discussion of the modification of structural, mechanical, and interband optical properties to specific studies [35,36]. We refer to donor atoms which effectively contribute to an increase in the charge-carrier density in the material as *activated dopants* (i.e., ionized) with volume density N_A, while *inactivated dopants* with density N_I designate P atoms that are incorporated into the crystal structure but do not contribute any free carrier. Secondary ion mass spectrometry (SIMS) is used to determine the total P atom concentration $[P] = N_A + N_I$ but transport or optical techniques are required to measure the activation ratio $N_A/[P]$. Basic theory of solid-state solutions tells us that active dopants are those that substitute to Ge in a lattice position, while donor atoms that occupy interstitial sites or phase separate into clusters are usually inactivated. It is well known that at high doping levels other effects take place, among them dopant-dimer formation [33], increase of the dislocation density, and clustering of dopants around crystal defects [36]. All these effects contribute to the decrease of $N_A/[P]$. Inactivated dopants generally act as neutral impurities weakly contributing to scattering of free carriers. On the other hand, in principle at high doping levels one has $N_A \simeq n$ and, since for mid-IR plasmonics n requires to be as high as possible, these unavoidable charged impurities represent a major contribution to electron scattering.

The thin-film growth is performed in a low-energy plasma-enhanced chemical vapor deposition (LEPE-CVD) reactor [37]. Therein, argon gas is introduced into the growth chamber after passing through a plasma source, where a tantalum filament is heated for thermionic emission. A dc arc discharge of 30 to 50 A is sustained between the filament and the growth chamber with a low voltage of 30 V and stabilized by an anode ring mounted in the growth chamber. Magnetic fields are used to focus the plasma onto the substrate heated up to a temperature T_{sub}. The deposition chamber has a base pressure of 10^{-9} mbar, while the working pressure reaches 10^{-2} mbar. The flow of precursors gases (GeH_4 for germanium, PH_3 and B_2H_6 for dopants, diluted in Ar) introduced in the chamber is regulated by mass flow controllers. The growth rate, controlled by the plasma density and by the flow of process gas, and the mobility of the adatoms, controlled by T_{sub}, can be optimized separately. A list of the samples grown and characterized in this work is reported in Table I. In this work, we used a growth mode featuring arc discharge current of 30 A, magnetic field of 1 mT, $T_{sub} \simeq 500\,^{\circ}C$ and GeH_4 flux kept at 20 sccm. In the 864× sample series, grown on (001) silicon wafers, the PH_3 flux was varied in percentage of its maximum value around 1 sccm. In the 933× series, the PH_3 flux was kept at 25% or 40% and three types of substrates were employed: (i) (001) germanium wafer for homoepitaxial growth resulting in threading dislocation densities in the n-Ge films $<10^5$ cm^{-2}; (ii) (001) silicon wafers for heteroepitaxial growth (due to the 4.2% difference between the lattice constants of Si and Ge) of fully relaxed n-Ge films with high dislocation densities of the order of 10^9 cm^{-2}; (iii) (001) silicon wafers with a 2-μm-thick undoped Ge layer (so-called *virtual substrate*) which is cyclically annealed between 600 °C and 780 °C to reduce the dislocation density down to 10^7 cm^{-2} before growing the n-doped film [38]. Indeed, heavily doped n-Ge films cannot be annealed at these temperatures because of the

TABLE I. Thickness, phosphorous atom density, and free-carrier density of n-Ge thin-film samples as determined by IR spectroscopy and other techniques (see text).

Sample	PH_3 flux	Substrate	d (μm)	d_{IR} (μm)	[P] (cm^{-3})	ρ_0 (Ωcm)	n_H (cm^{-3})	n_{IR} (cm^{-3})	n_{IR}/[P]
8648	1%	Si wafer	1.39	1.30	2.0×10^{17}	4.5×10^{-2}	1.4×10^{17}	2.1×10^{17}	100%
8643	10%	Si wafer	1.45	1.33	3.6×10^{18}	2.5×10^{-3}	3.4×10^{18}	3.5×10^{18}	97%
8649	25%	Si wafer	1.18	1.00	1.3×10^{19}	1.4×10^{-3}	1.0×10^{19}	1.1×10^{19}	85%
8644	30%	Si wafer	1.15	0.97	2.1×10^{19}	1.0×10^{-3}	1.5×10^{19}	1.5×10^{19}	71%
9007	50%	Si wafer	1.00	0.99	7.5×10^{19}	5.5×10^{-4}	2.6×10^{19}	2.5×10^{19}	33%
9332	25%	Si wafer	2.0	2.5	1.3×10^{19}	8.1×10^{-4}	0.9×10^{19}	0.8×10^{19}	62%
9338	40%	Si wafer	2.0	2.3	3.5×10^{19}	4.3×10^{-4}	2.5×10^{19}	2.3×10^{19}	66%
9335	40%	Virtual Ge	2.0	2.1	3.5×10^{19}	5.9×10^{-4}	2.9×10^{19}	2.5×10^{19}	71%
9336	40%	Ge wafer	2.0	2.1	3.5×10^{19}	9.1×10^{-4}	3.3×10^{19}	3.0×10^{19}	86%

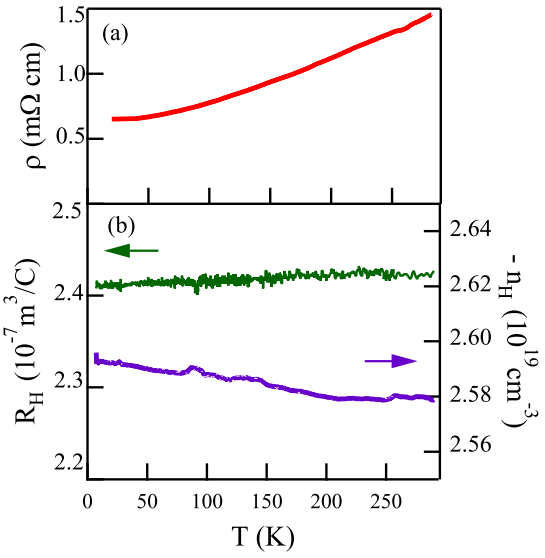

FIG. 3. The measured Hall coefficient (left scale) and the calculated Hall carrier density (right scale) of sample 9007 as a function of temperature. The slight difference between the expression $-1/eR_H$ and n_H is due to consideration of the Hall factor at all T's.

tendency of P atoms to form clusters [36]. SIMS measurements have been performed to quantify the total P-atom incorporation by using a CAMECA ims-4f mass spectrometer. An O_2^+ ion beam with accelerating voltage of 8 keV, rastered over a 250×250 μm^2 area, was used for sputtering, while collecting $^{31}P\,^{16}O^+$ secondary ions. Calibration of [P] was performed by measuring a Ge standard with known P areal density with an accuracy of $\pm15\%$. The concentration levels within the n-Ge films resulted to be uniform to within $\pm5\%$.

Temperature- (T-) dependent dc transport measurements have been performed in order to determine the dc resistivity $\rho(T)$ and the Hall coefficient $R_H(T)$. As shallow defects can be thermally activated even at room T to increase the measured transport carrier density, it is important to undertake T-dependent Hall measurements to determine the activated carrier density. For samples from the 933× series, data were acquired at all T from 5 to 300 K with a step of 0.1 K/s. For the 864× series, the measurements were performed only at $T =$ 300 K. All dc transport data were collected from six-terminal Hall bars processed by UV lithography and dry etching. A Ni/Ti/Al (100 nm/5 nm/100 nm) metal stack was evaporated on the electrical pads and then annealed at 340 °C for 30 s in order to create low-resistivity Ohmic contacts [39]. The temperature dependence of $\rho(T)$ has been found to be almost linearly dependent on T from 300 to 50 K for all samples. $R_H(T)$ measured applying a magnetic field of 2.5 T displayed a constant value, different for each sample, over the full temperature range. An example is shown in Fig. 3 for sample 9007 grown on an intrinsic Si substrate. This is expected because all samples of the 933× series are doped close or beyond the level of the Mott transition in Ge ($N_{Mott} \simeq 2.5\times10^{17}\,cm^{-3}$) [40–42]. The measured value of R_H was used to determine the Hall carrier density $n_H = -1/eR_H$ reported in Table I [43]. An estimate of the scattering time from dc transport measurements is calculated from $\tau_{dc}(T) = m^*[n_H e^2 \rho(T)]^{-1}$ [44]. This value can be used for a first-step evaluation of losses in mid-IR plasmonics, as is often undertaken in the literature [12]. In the group-IV elemental semiconductors Ge and Si, however, electron dynamics are dominated by the deformation potential scattering due to the lack of polar optical phonons [45]. The deformation potential scattering is weakly T dependent and strongly ω dependent, therefore, the determination of losses in n-Ge plasmonic resonators cannot be based on dc transport only, but a direct determination of the dielectric function at IR frequencies is needed.

II. DIELECTRIC FUNCTION DETERMINATION

Reflection spectroscopy performed at all ω from the far-IR to the near-IR provides a wealth of information on heavily doped semiconductor thin films, which complements the transport properties. The ω- and T-dependent absolute normal-incidence reflectivity $R(\omega)$ was measured in the 50 $cm^{-1} < \omega <$ 6000 cm^{-1} range with a Michelson-type Fourier-transform spectrometer (Bruker IFS66v) equipped with a suite of beam splitters and two cryogenic detectors: a HgCdTe photovoltaic detector from Infrared Associates, whose response was linearized for different power levels, and a 4-K silicon bolometer from Infrared Labs, which features linear responsivity. The beam from the Michelson interferometer is sent to a homemade purely normal-incidence reflectivity setup based on the insertion of a broadband beam splitter that conveys to the detectors around half of the beam reflected by the sample, which was glued on a copper ring and kept in a liquid-helium flow cryostat. Reference spectra were acquired at all T and ω on a gold mirror, also kept in the cryostat and displaced exactly at the position previously occupied by the sample. The absolute reflectivity of all samples and also of bare substrates was obtained by dividing the sample spectrum by the reference spectrum taken with the same optical path alignment. The merged $R(\omega)$ data sets for the 864× and 933× series at room T are shown in Figs. 4 and 5, respectively. Aside from the sinusoidal oscillations due to Fabry-Perot interference in the Ge film, one sees that the plasma edge moves to higher frequency for higher n as expected from Eq. (1). In Fig. 6, the low-T spectrum is also shown for two samples: the position of the plasma edge does not change appreciably with cooling, in agreement with the measured T-independent value of $n_H(T)$.

Silicon wafers in use in the electronic industry, here employed as substrates for CVD growth, display different types of IR-active impurity state transitions resulting in narrow spectral features that impact on the mid-IR transmission spectrum of the multilayer formed by the film and the much thicker substrate. For this reason, in our experiment we measure instead $R(\omega)$ which, for thick enough films is mainly determined by the optical properties of the CVD-grown n-Ge film. From the Fresnel relations at exactly normal incidence, we can write

$$R(\omega) \simeq \left| \frac{r_{12} + r_{23} e^{2i\beta(\omega)} e^{-\alpha(\omega) d_{IR}}}{1 + r_{12} r_{23} e^{2i\beta(\omega)} e^{-\alpha(\omega) d_{IR}}} \right|^2, \qquad (2)$$

where r_{jk} are the ω-dependent complex Fresnel reflection coefficients of the different interfaces, the subscripts 1, 2, and 3 refer to vacuum, n-Ge film, and Si substrate, respectively, the subscript pair indicates the corresponding

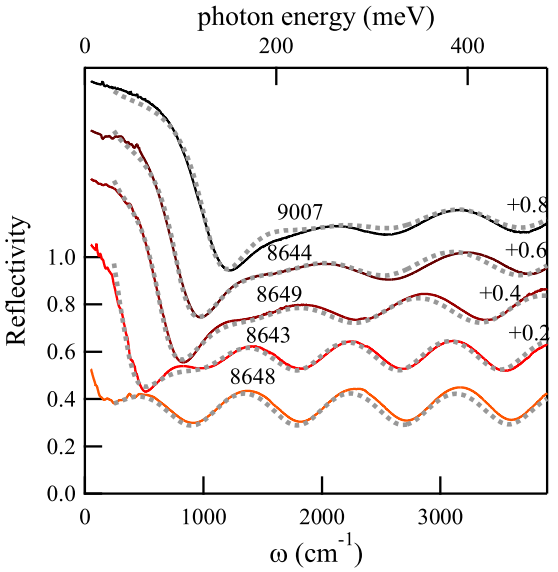

FIG. 4. The absolute reflectivity at room T of n-Ge thin films of thickness $\sim$1 μm, grown on silicon wafers with varying PH_3 flux (see Table I). The dashed lines are calculated from the best fit of the Drude-Lorentz dielectric function of n-Ge [Eq. (2)] to the data. Curves are offset for clarity, the offset value is indicated on the right.

interface, $\beta = 2\pi\eta(\omega)d_{\rm IR}/\lambda$ is the phase delay accumulated while traveling through the n-Ge film and $\alpha(\omega)$ is the n-Ge absorption coefficient, and $d_{\rm IR}$ is the IR thickness which,

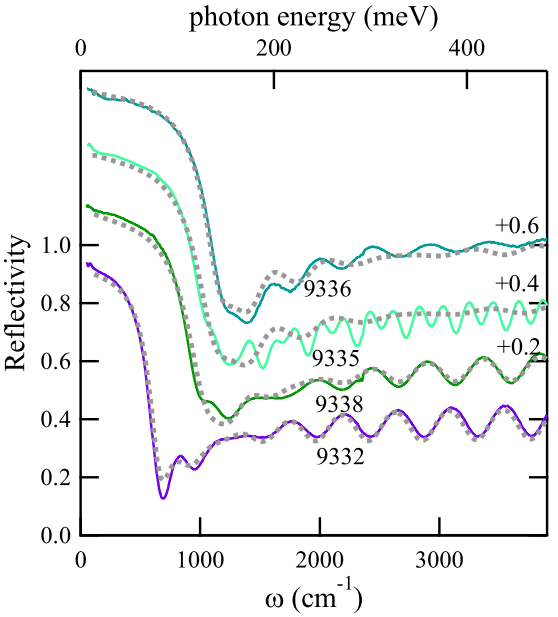

FIG. 5. The absolute reflectivity at room T of n-Ge thin films of thickness $\sim$2 μm grown on different substrates (see Table I). The dashed lines are calculated from the best fit of the Drude-Lorentz dielectric function of n-Ge [Eq. (2)] to the data. The model does not include the virtual substrate interface to the wafer, therefore, it cannot reproduce the oscillations seen in the data of sample 9335 above $\sim$1500 cm^{-1}, but this is inessential for the determination of the free-carrier parameters. Curves are offset for clarity, the offset value is indicated on the right.

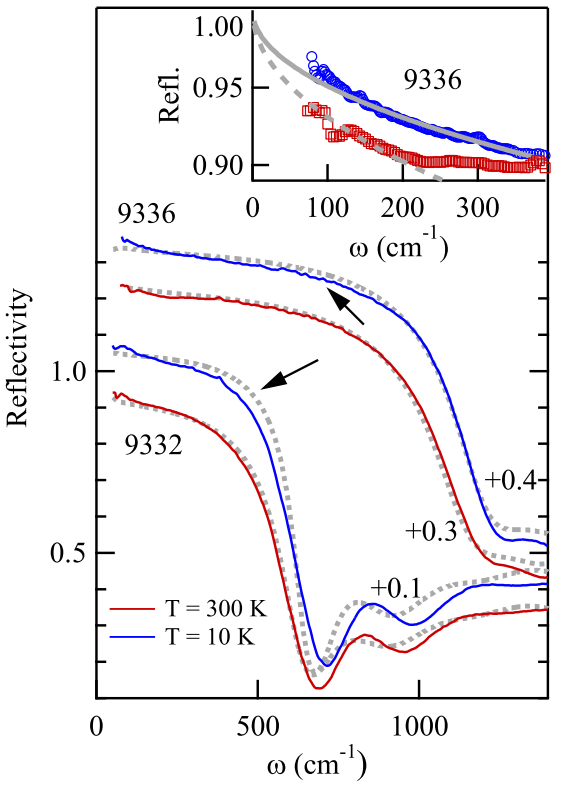

FIG. 6. Drude-Lorentz fitting (dotted gray lines) is possible for the reflectivity data measured at $T = 300$ K (red, offset 0 and +0.3 for samples 9332 and 9336, respectively) but not possible for the same data at $T = 10$ K (blue, offset 0.1 and 0.4): the black arrows indicate the frequency ranges where the data at $T = 10$ K and the model do not overlap. In the inset, enlarged view of the far-IR data of sample 9336 at $T = 10$ K (circles) and at $T = 300$ K (squares) with the Hagen-Rubens fit (thick gray lines).

at first order, equals the physical thickness. The backside substrate-vacuum interface is not included in Eq. (2) because it is left unpolished. In the far-IR, for a large enough value of the product $\alpha(\omega)d_{\rm IR}$, one has $R(\omega) \simeq |r_{12}|^2$ and the Si substrate properties, which enter only in r_{23}, do not contribute to the reflected intensity spectrum. The condition $\alpha(\omega)d_{\rm IR} \gg 1$ was self-consistently checked after the determination of the dielectric function [see inset of Fig. 7(c)]. For ω above the plasma edge ($\sim$1000 cm^{-1}), the condition $\alpha(\omega)d_{\rm IR} \gg 1$ does not hold and the dielectric function of the Si substrate measured in a separate reflection/transmission experiment was used as a fixed input to reduce the number of free parameters. For $\omega > 1000$ cm^{-1}, we found $\epsilon_{\rm Si} \sim 11.9 + 0.1i$ for our wafers. The unknown dielectric function of the n-Ge film is modeled with a multioscillator Drude-Lorentz expression (here and everywhere in the paper, the frequency ω and the scattering rates γ_i are expressed in the practical units cm^{-1}, while $\hbar$ is expressed in eV $\cdot$ cm):

$$\tilde{\epsilon}(\omega) = \epsilon_\infty - \frac{\omega_p^2}{\omega^2 + i\omega\gamma_{\rm D}} + \sum_{i=1}^{2} \frac{S_i^2}{(\omega_i^2 - \omega^2) - i\omega\gamma_i} \qquad (3)$$

from which all the response functions in Eq. (2) (r_{12},r_{23},η,α) are determined by classical electrodynamics relations [46]. A

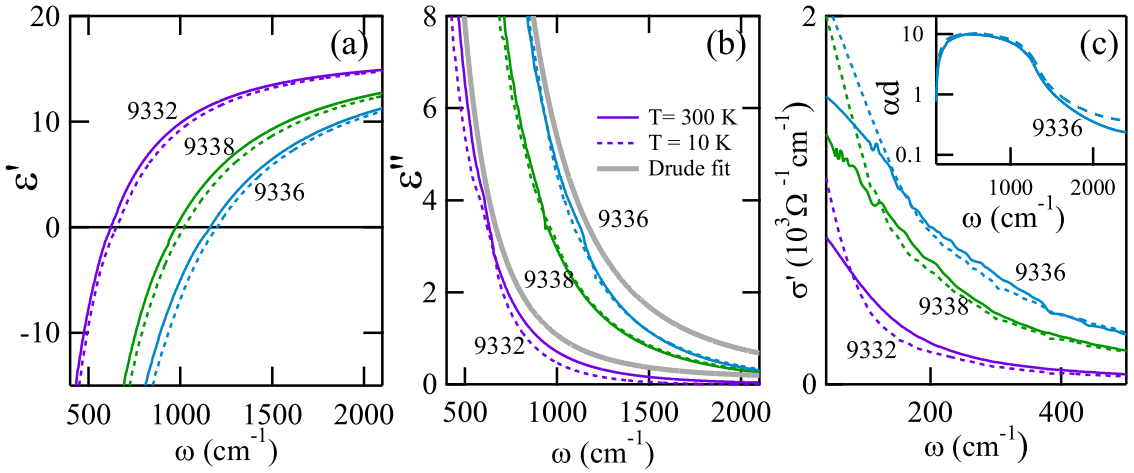

FIG. 7. (a), (b) Dielectric function and (c) optical conductivity as determined by the Kramers-Kronig transformations for samples 9332, 9338, and 9336. Solid lines: $T = 300$ K, dashed lines: $T = 10$ K. In panel (b), $\epsilon''(\omega)$ calculated with the Drude-Lorentz formula and best-fit parameters for samples 9332 and 9336 is also shown (thick gray lines): clearly, the model does not reproduce the mid-IR data of sample 9332 (9336) for $\omega \gtrsim 700$ (1000) cm^{-1}. In the inset of panel (c), the product $\alpha(\omega)d_{\mathrm{IR}}$ for sample 9338 is much larger than unity in the range of interest, validating the KK analysis based on semi-infinite medium approximation in a self-consistent way.

fit to Eq. (3) provides the unknown free-carrier parameters (the *Drude weight* ω_p^2 and the *Drude scattering rate* γ_{D}) while $\epsilon_\infty = 16.0$. The frequency of the interband transitions is approximately known ($\hbar\omega_1 = 0.66$ eV for the indirect gap transition, and $\hbar\omega_2 = 0.84$ eV for the direct gap transition at room T), and the parameters S_1, S_2 and γ_1, γ_2 display almost the same values for all samples. Notice that the *unscreened* plasma frequency ω_p is now defined as the square root of the Drude weight, and it is conceptually different from ω^* defined previously. ω_p is the absorption cross section of the free carriers which depends only on $\sqrt{n/m^*}$ and not on screening. ω^* is the highest frequency where metallic behavior is observed ($\epsilon' < 0$), hence, it also depends on the screening field produced by the valence electrons, which is approximately accounted for by using $\epsilon_\infty > 1$.

As explained in the introduction, n-Ge features a band structure that allows for an approximate description of its dielectric response in terms of the Drude term only [the first term of Eq. (3)], as is usually undertaken in the applied physics literature [47]. The consequence of simplifying the Drude-Lorentz model to an effective Drude-only model is the use of a phenomenological value for the infinity dielectric constant that we accurately determined to be $\epsilon_\infty^* = 16.6 > 16.0$ in our case. The slightly higher value of ϵ_∞^* if compared to the nominal undoped-Ge dielectric permittivity value 16.0 accounts for the extra screening of free-carrier oscillations by dipole moments of the interband transitions, which are slightly stronger in doped materials because crystal defects enhance the dipole moment of the indirect-gap transition [48]. Samples with high crystal defect densities and strongly enhanced interband transition strengths have demonstrated values of ϵ_∞^* up to 18 (not reported here). Noticeably, the best-fit Drude-only parameters ω_p and γ_{D} coincide within errors (around $\pm 2\%$) with those of the Drude-Lorentz fit. A more accurate value of ω^* at room T can then be obtained from the condition $\epsilon'(\omega^*) = 0$ that simply gives

$$\omega^* = \sqrt{\frac{\omega_p^2}{\epsilon_\infty^*} - \gamma_{\mathrm{D}}^2} \tag{4}$$

and provides a direct estimate of ω^* from the Drude-only fitting parameters. Only in the zero-loss limit $\omega_p \gg \gamma_{\mathrm{D}}$, the above expression reduces to the approximate relation for the screened plasma frequency [Eq. (1)]. One can see that, due to losses, the difference between Eqs. (4) and (1), the latter commonly employed in the plasmonics literature [12], is not negligible in many of the materials considered for mid-IR plasmonics applications.

A. Infrared estimate of the free-carrier density

We now turn to the determination of the free-carrier concentration n from the Drude weight ω_p^2:

$$n_{\mathrm{IR}} = \frac{\omega_p^2 m^*}{4\pi\epsilon_0 e^2}. \tag{5}$$

A procedure based on the determination of the zero-crossing frequency of $\epsilon'(\omega)$ by mid-IR spectroscopic ellipsometry and the subsequent retrieval of ω_p^2 through Eq. (4) by using estimates for ϵ_∞^* and γ_{D} has been recently employed on n-Ge films [47]. We have already seen, however, that the estimate of ϵ_∞^* is not straightforward even in the case of well-known semiconductors like Ge. We will also see below that, in heavily doped materials, the parameter γ_{D} represents only a rough estimate of the actual mid-infrared losses. Instead, fitting either the Drude-Lorentz or the Drude-only model to the entire far- to near-IR $R(\omega)$ almost eliminates the dependence of the relevant parameter ω_p on ϵ_∞^* and γ_{D}. The uncertainty of n_{IR} is around $\pm 4\%$ propagated from the uncertainty in the fitting parameter ω_p of $\pm 2\%$, and it is not limited by the smaller

TABLE II. *n*-Ge parameters relevant for mid-IR plasmonics.

	T independent			$T = 300$ K			$T = 10$ K		
Sample	ω_p (cm^{-1})	n_{IR} (cm^{-3})	$(2\pi c\gamma_D)^{-1}$ (ps)	ω^* (cm^{-1})	τ_{IR} (ps)	τ_{dc} (ps)	ω^* (cm^{-1})	τ_{IR} (ps)	τ_{dc} (ps)
8648	390	2.1×10^{17}	0.026			0.064			
8643	1600	3.5×10^{18}	0.026	310	0.025	0.047			
8649	2840	1.1×10^{19}	0.026	666	0.015	0.029			
8644	3310	1.5×10^{19}	0.026	815	0.014	0.027			
9007	4280	2.5×10^{19}	0.017	1060	0.014	0.028			
9332	2450	0.8×10^{19}	0.026	620	0.027	0.055	650	0.055	0.077
9338	4200	2.3×10^{19}	0.021	970	0.019	0.037	1020	0.032	0.052
9335	4230	2.5×10^{19}	0.021	1050	0.018	0.023	1070	0.036	0.033
9336	4800	3.0×10^{19}	0.021	1160	0.018	0.013	1200	0.024	0.019

uncertainty on $m^* = 0.12$ [30]. The n_{IR} values determined from the Drude-only fit are reported in Tables I and II. One can see from Table I that the almost T-independent values of n_H are consistent with the values of n_{IR} determined at room T from the Drude weight for all samples. n_{IR}, however, is much less dependent on the substrate conductivity than n_H, and therefore it is used to determine the activation ratios reported in Table I. A further model-independent method to determine ω_p and then n from the IR data is provided by the oscillator strength sum rules [46], which can be applied only once the optical constants are calculated in the entire IR range by the Kramers-Kronig (KK) transformations, as done in Ref. [49] and below in this work.

B. Infrared estimate of the scattering time

We now turn to the comparison of τ_{dc} with the Drude scattering time $(2\pi c\gamma_D)^{-1}$ determined from the fitting routine at $T = 300$ K and reported in Table II, where c is the speed of light in a vacuum. While the values of the two quantities fall approximately in the same subpicosecond range for all samples, there is a strong dependence of τ_{dc} on n that has no counterpart in $(2\pi c\gamma_D)^{-1}$, which is doping independent. The reason is that τ_{dc} is mainly determined by the electron momentum-relaxation process through electron scattering events with vanishing energy exchange, including elastic scattering with impurities, while $(2\pi c\gamma_D)^{-1}$ is the inelastic scattering time of oscillating electron currents, taken as constant in a broad range of IR frequencies of the order of γ_D itself. The main inelastic mechanism is electron-phonon scattering that does not depend on the electron density and this explains the doping independence of γ_D. It should also be noted that the scattering times τ_{dc} and $(2\pi c\gamma_D)^{-1}$ are determined from processes that display very different dependence on the scattering angle [50]. However, one could still argue that electron momentum and energy relaxation processes are linked to each other and, therefore, there should exist a limit for $\omega \to 0$ where optical and transport scattering time approximately coincide. Indeed, this limit exists and it is represented by the empirical Hagen-Rubens relation between the normal-incidence reflectivity and the dc conductivity $\sigma_{dc} = 1/\rho = ne^2\tau_{dc}/m^*$, which holds for good conductors in the frequency range where the imaginary part of $\tilde{\sigma}(\omega)$ is negligible if compared to the real part [46]:

$$R(\omega) = 1 - A(\omega) \simeq 1 - \sqrt{A_{HR}\omega} = 1 - \sqrt{\frac{2\omega}{\pi\sigma_{dc}}}, \qquad (6)$$

where $A(\omega) \simeq \sqrt{A_{HR}\omega}$ is the emittance of the semi-infinite medium [46]. We can fit Eq. (6) to our reflectivity data in the far-IR range $\omega \lesssim 200$ cm^{-1} to determine the coefficient A_{HR} [see inset of Fig. 6, from which we calculate a low-frequency scattering time $\tau_{IR} = 8A_{HR}/\omega_p^2$ using the value for the Drude weight derived from the Drude-Lorentz model (5) and the relation $\sigma_{dc} = ne^2\tau/m^*$]. As seen from Table II, the value of τ_{IR} is similar to that of $(2\pi c\gamma_D)^{-1}$, but it decreases with increasing doping like τ_{dc}.

C. Infrared estimate of the film thickness

The best-fit value of d_{IR} is reported in Table I and it is mainly determined by the Fabry-Perot fringe pattern visible in $R(\omega)$ above the screened plasma frequency. The reason for the discrepancy of ~15% between d_{IR} and the physical thickness d as measured by cross-sectional scanning electron microscopy is unclear at the moment, and it could be due either to experimental uncertainties in d or to nonideality of the optical setup such as the finite distribution of incidence angles around the normal direction that affected the absolute level of $R(\omega)$, or both, as well as to the failure of the smooth optical interface model, or finally to the non-Lorentzian shape of the indirect-gap absorption feature at 5500 cm^{-1}.

D. Low-temperature electrodynamics

We have found that the Drude-Lorentz model reasonably reproduces $R(\omega)$ at $T = 300$ K. The situation is completely different when one turns to the low T $R(\omega)$. If one looks at the data taken at $T = 300$ and 10 K (thin colored lines in Fig. 6), one sees that the plasma edge does not shift appreciably, as expected from the fact that n is constant with T. At the same time, the low-frequency value of $R(\omega)$ increases in the entire far-IR range with cooling, which is consistent with a reduction of the electromagnetic field penetration depth (skin depth) due to decrease of free-carrier losses. The best fit of Eq. (2) to the $R(\omega)$ data at low T, however, based on the Drude model of Eq. (3), is not possible because there is no single value of the fit parameter $\gamma_D(10\text{ K})$ that reproduces both the increased far-IR

reflectance (see also the inset of Fig. 6) and the substantial insensitivity to T of the slope of the plasma edge in the mid-IR. This is clearly demonstrated by the dashed gray lines in Fig. 6 obtained by imposing a value constant with T for the product $\gamma_D \cdot \tau_{dc}$: in a broad range of frequencies, indicated by the black arrows, there is no overlap between the data and the model. It is possible to reproduce $R(\omega)$ at low T by decreasing the Drude weight and by adding several Lorentz oscillators in the far-IR representing photoionization of weakly bound charges. Decreasing the Drude weight at low T, however, would conflict with the T-independent free-carrier density established from both the Mott criterion and the observed T independent n_H.

The failure of the Drude model in reproducing the $R(\omega)$ spectra at $T = 10$ K, together with the above-mentioned inconsistency between τ_{IR} and $(2\pi c\gamma_D)^{-1}$ at $T = 300$ K, indicate that the interpretation of energy relaxation using a single characteristic electron scattering time is not valid in heavily doped semiconductors, as already pointed out from theory [51]. Indeed, it is well known that the Drude model reproduces the IR data in limited IR frequency ranges only [52]. Instead, for a correct electrodynamic description of electron scattering, one should use (at any T) the frequency-dependent scattering rate $\gamma(\omega)$. Conceptually, $\gamma(\omega)$ includes the dependence of the electron scattering cross section on energy and the frequency-dependent joint density of states (JDOS), i.e., the product of the density of occupied initial states and unoccupied final states separated by a given energy step. These effects cannot be ignored in heavily doped semiconductors because their Fermi level is close to the minimum of a parabolic band leading to a strong dependence of the JDOS on the electron energy. Moreover, the electron-energy dependence of the scattering cross section is strong in the case of (inelastic) optical phonon scattering. Therefore, the values of γ_D used to reproduce a subset of the IR data within the Drude model are to be interpreted as the average value of $\gamma(\omega)$ in that specific frequency range (see, e.g., Ref. [52]). In the far-IR for $\omega \to 0$, momentum and energy relaxation processes cannot be clearly distinguished and, therefore, one finds $\tau_{IR} < (2\pi c\gamma_D)^{-1}$. In the next two subsections, we describe a procedure to determine $\gamma(\omega)$ at all frequencies from the IR data in a model-independent way.

E. Kramers-Kronig analysis

In the Kramers-Kronig (KK) transformation analysis, the electrodynamic response function is determined from the IR reflectance data in a model-independent way. The film is assumed to be semi-infinite and the phase $\theta(\omega)$ of the Fresnel reflection coefficient $r_{12}(\omega)$ is retrieved by applying KK transformations to $|r_{12}(\omega)| = \sqrt{R(\omega)}$. With the complex semi-infinite medium reflectance $\tilde{r}_{12}(\omega)$ at hand, one can calculate all other optical response functions of n-Ge as a function of frequency [46], including the optical conductivity $\tilde{\sigma}(\omega)$, the dielectric function $\tilde{\epsilon}(\omega)$, and the memory function $\tilde{\gamma}(\omega)$ (see below). To perform the KK analysis, one needs to extend the ω dependence of the data outside the experimentally available range. For $\omega \to 0$, we extrapolated the merged $R(\omega)$ data sets with the Hagen-Rubens formula of Eq. (6). For $\omega \to \infty$, we substituted the $R(\omega)$ data above the plasma edge (where the film becomes partly transparent) with the Drude-Lorentz model reflectivity calculated from Eq. (2) in the limit $d_{IR} \to \infty$. This procedure is explained in details in Ref. [53]. The resulting optical constants are accurate to within 5% in the frequency range $(2\pi c\tau_{IR})^{-1} < \omega < \omega^*$. In Fig. 7, we plot the resulting dielectric function of the 933× series at $T = 10$ and 300 K. The data of sample 9335 are not reported for clarity as they overlap to those of sample 9338. Continuous lines are the $T = 300$ K values while dashed lines are the $T = 10$ K values: it is apparent that, while the real part $\epsilon'(\omega)$ shows a small T dependence, the imaginary part $\epsilon''(\omega)$ at the two T's almost overlap, indicating that the decrease of the dc mobility with cooling has a very weak effect on the mid-IR dielectric function close to ω^*. This fact is better highlighted by plotting in Fig. 7(c) the real part of the optical conductivity $\sigma' = (-i\omega\epsilon_0/4\pi)\epsilon''$, which only at low ω is significantly T dependent. The Drude weight ω_p determined from the Drude-only fit coincides within 5% with the result of the oscillator strength sum rule [frequency integral of σ' in Fig. 7(c)] at both 300 and 10 K. The data in Fig. 7 differ considerably from the dielectric function obtained by the Drude-Lorentz and Drude-only models [see Fig. 7(b)]. They can be considered an almost model-independent estimate of the dielectric function for n-Ge at all frequencies to be used for electromagnetic design.

We can now summarize the optical parameters of n-Ge relevant for mid-IR plasmonics in Table II. The value of ω^* is here directly determined from the dielectric function resulting from KK analysis by searching the frequency where $\epsilon'(\omega^*) = 0$ in Fig. 7(a), instead of using the approximate relation of Eq. (1) or the model-dependent relation of Eq. (4). The values of ω^* at both 10 and 300 K coincide within ±5% with the respective T-independent values of $\omega_p/\sqrt{\epsilon_\infty}$, confirming that the Drude weight parameter of the Drude-Lorentz model provides a good estimate of the free-carrier density, even if the same model fails to accurately reproduce the dielectric function and the scattering rate. Also, ω^* obtained from the KK analysis increases slightly with cooling, an effect that can be derived neither from Eq. (1), where all quantities are constant with T, nor from Eq. (4), where γ_D is undefined at low T. The weak but clear dependence of ω^* on T reflects the slight decrease of electron energy losses in the mid-IR with cooling, due to the decrease of thermal population of optical phonons. Turning to the loss parameters, the Hagen-Rubens scattering time τ_{IR}, determined from the zero-frequency extrapolation of $R(\omega)$, is approximately similar to τ_{dc} and, therefore, it is determined by both momentum energy relaxation processes with small energy exchange and energy relaxation processes. Instead, the Drude scattering time $(2\pi c\gamma_D)^{-1}$ is longer than both τ_{IR} and τ_{dc} because it is mainly determined by inelastic electron-phonon scattering (red arrow in Fig. 1), and not much by elastic charged-impurity scattering (black arrow in Fig. 1). Indeed, γ_D in Table II is almost doping independent. This fact suggests that γ_D is not a good parameter to estimate plasmon losses which are certainly due also to momentum relaxation by charged-impurity scattering (black arrow in Fig. 1). The estimate of mid-IR plasmon losses instead requires both the evaluation of the frequency-dependent scattering rate and the calculation of the total (elastic and inelastic) frequency-dependent average electron scattering cross sections, presented in the next sections.

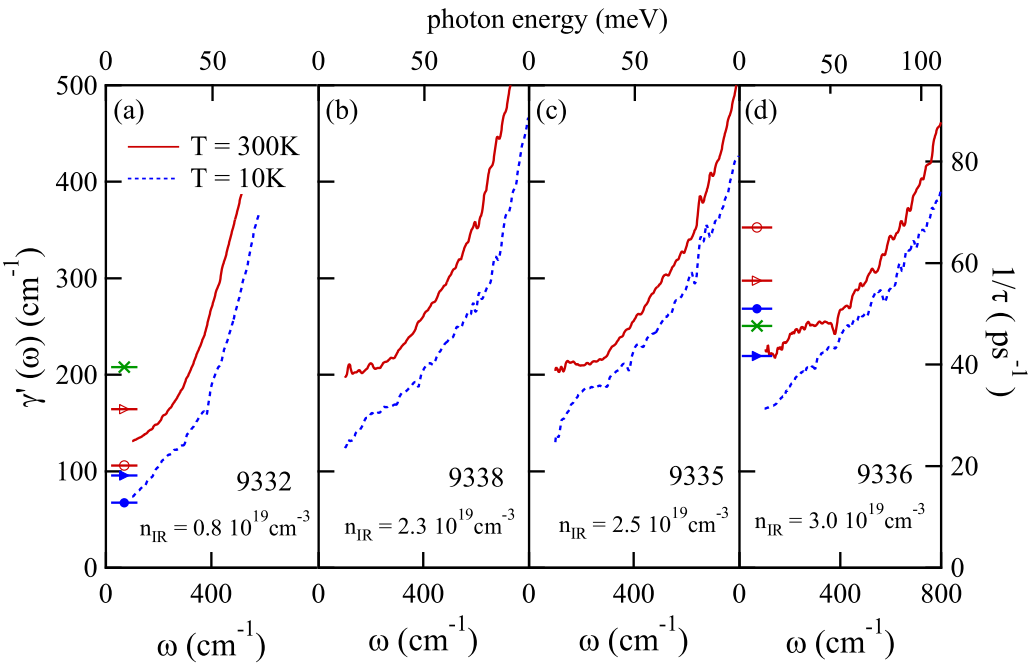

FIG. 8. The model-independent experimental frequency-dependent average electron scattering rate $\gamma'(\omega)$ calculated from the optical conductivity according to Eq. (7) reported in the text. The symbols in panels (a) and (d) correspond to inverse scattering time values (right scale) obtained from different charge-transport models for $2\pi c\gamma_D^{-1}$ (green cross), τ_{IR}^{-1} (triangles), and τ_{dc}^{-1} (circles). Empty symbols are for $T = 300$ K values, full symbols for values at $T = 10$ K. Numerical values are reported in Table II.

F. Frequency-dependent scattering rate

The Drude model of the free-carrier electrodynamics can be naturally extended to include the dependence of electron energy relaxation processes on ω by making the scattering rate of the Drude formula ω dependent (and therefore complex in order to satisfy its own KK relations). $\tilde{\gamma}(\omega)$ is one of the equivalent forms of the electrodynamic response function. It can be demonstrated [54,55] that $\tilde{\gamma}(\omega)$ is related to $\tilde{\sigma}(\omega)$ as follows:

$$\begin{aligned}\tilde{\gamma}(\omega) &= \gamma'(\omega) + i\gamma''(\omega),\\ \gamma'(\omega) &= \frac{\omega_p^2}{4\pi}\mathrm{Re}\left(\frac{1}{\tilde{\sigma}(\omega)}\right),\\ \gamma''(\omega) &= -\frac{\omega_p^2}{4\pi\omega}\left[\mathrm{Im}\left(\frac{1}{\tilde{\sigma}(\omega)}\right) - 1\right].\end{aligned} \tag{7}$$

This so-called extended Drude model has been employed to analyze the electrodynamics in the IR range of metals [56–59], transition-metal compounds [54], heavy-fermion systems [60], and high critical temperature cuprate superconductors [61]. The real part $\gamma'(\omega)$ represents the ω-dependent electron scattering rate averaged over all electrons occupying states within an energy shell $\pm\hbar\omega$ from the Fermi level, and normalized by the electron density. As such, $\gamma'(\omega)$ can be used for an approximate evaluation of the energy relaxation rate of a finite-frequency collective electron excitation (plasmon at ω) interacting with the crystal lattice. Writing $\tilde{\sigma}(\omega) = (4\pi i/\omega)^{-1}[\tilde{\epsilon}(\omega) - \epsilon_\infty]$, one can express $\gamma'(\omega)$ in terms of the complex dielectric function:

$$\gamma'(\omega) = \frac{\omega_p^2}{\omega}\frac{\epsilon''(\omega)}{[\epsilon'(\omega) - \epsilon_\infty]^2 + [\epsilon''(\omega)]^2}, \tag{8}$$

where we can input the data shown in Fig. 7 and obtain an experimental $\gamma'(\omega)$ to be compared with the ω-dependent scattering cross section determined from first principles (see next section). For completeness, we mention that the imaginary part of $\tilde{\gamma}(\omega)$ represents the frequency-dependent effective-mass renormalization factor. The relation between $\gamma''(\omega)$ and $\tilde{\epsilon}(\omega)$ can be derived similarly to Eq. (8), but it is not of interest here.

In Fig. 8, we plot $\gamma'(\omega)$ at $\omega \lesssim \omega^*$ for the four samples that were studied as a function of T. It increases with ω at both room T and low T for all doping levels, due to the increase of both the density of available final states for processes with high-energy exchange $\pm\hbar\omega$ and the electron-phonon scattering cross section with increasing excess energy of the electrons above the Fermi level, as it will be clarified in the next section. The increase of $\gamma'(\omega)$ with ω is very important for the evaluation of mid-IR plasmonic losses because it indicates that they are generally underestimated when the scattering time determined from dc transport is employed. We point out two further experimental facts: (i) $\gamma'(\omega)$ is always higher at room T than at low T for each sample, indicating the key role played by absorption of thermally excited phonons; (ii) $\gamma'(\omega)$ does not decrease in sample 9336 which is homoepitaxially grown on a Ge wafer hence has fewer crystal defects if compared to the other samples grown on Si wafers, therefore, it does not depend on the crystal defect density.

III. MODEL OF ELECTRON SCATTERING

The electron scattering rate in heavily doped n-type Ge has been estimated theoretically in single-particle effective-mass approximation as a function of the excess kinetic energy of carriers at the L point in $\mathbf{k}$ space. This was done by means of first-order perturbation theory, taking into account both elastic and inelastic processes. Scattering rates have been obtained considering the ellipsoidal character of the band dispersion close to fourfold degenerate L minima. We include in the model the (inelastic) interaction of carriers with optical phonons and the (elastic) scattering events related to the presence of charged-impurity centers (activated dopant atoms with density N_A). We will also discuss the carrier scattering due to the interaction with acoustic phonons, neutral impurities (inactivated dopant atoms of density N_I), and crystal defects, in order to motivate our choice of neglecting these contributions in the evaluation of the total electron scattering rate.

Optical phonons. The nonpolar character of the Ge lattice does not allow for the existence of IR-active optical phonon modes whose dipolar field directly interacts with free carriers [50]. Indeed, $\epsilon''(\omega)$ in Fig. 7 does not present any absorption resonance at the optical phonon frequencies. In an ideal nonpolar crystal, however, there is a residual short-range electromagnetic interaction between electrons and lattice ions, due to thermal excitation of the lattice, which drives the ions outside of their equilibrium position, known as deformation potential scattering [50]. At low T where thermal fluctuations are small, the scattering is possible only via phonon emission for electrons whose excess energy with respect to the band edge is higher than the phonon energy. At higher T, also phonon absorption processes, involving in principle electrons with arbitrary excess energy, become relevant. Both phonon absorption and emission processes have a significant dependence on T because they are governed by the Bose-Einstein distribution function for the phonon population at a given T. On the other hand, the doping level influences to a minor extent the electron-phonon scattering, although it is true that the number of electrons with sufficient kinetic energy to emit optical phonons increases with the Fermi level E_F.

We first calculate $W^{OP}(\mathbf{k}) = W^{OP_{abs}}(\mathbf{k}) + W^{OP_{em}}(\mathbf{k})$ defined as the scattering rate for an electron in the L valley with momentum $\mathbf{k}$ due to the absorption ($W^{OP_{abs}}$) or emission ($W^{OP_{em}}$) of an optical phonon. This term can be written as

$$W^{OP_{abs/em}}(\mathbf{k}) = \frac{2\pi}{\hbar}\sum_{\mathbf{k}'}|H_{\mathbf{k}\mathbf{k}'}|^2\delta(\varepsilon_{\mathbf{k}} - \varepsilon_{\mathbf{k}'} \pm \hbar\omega_{ph})(1 - f_{\varepsilon_{\mathbf{k}'}}), \tag{9}$$

where the upper/lower sign refers to phonon absorption/emission, $f_{\varepsilon_{\mathbf{k}'}}$ is the Fermi factor for the occupation probability of the final electronic state with momentum $\mathbf{k}'$, and $\hbar\omega_{ph}$ is the optical phonon energy, assumed to be momentum independent. The matrix element $H_{\mathbf{k}\mathbf{k}'}$ represents the electron-phonon interaction due to deformation potential coupling. Assuming an effective deformation potential D_{eff} which represents the joint action of all the active phonon branches, $H_{\mathbf{k}\mathbf{k}'}$ can be calculated as [62]

$$|H_{\mathbf{k}\mathbf{k}'}|^2 = \left(n_{ph} + \frac{1}{2} \mp \frac{1}{2}\right)\frac{\hbar^2 D_{eff}^2}{2\rho V \hbar\omega_{ph}}, \tag{10}$$

TABLE III. Effective optical phonon energy $\hbar\omega_{ph}$ and deformation potential D_{eff} according to Ref. [63].

	$\hbar\omega_{ph}$ (meV)	D_{eff} (10^8 eV/cm)
Intravalley L-L	37.04	3.50
Intervalley L-L	23.95	5.26
Inter-alley L-Γ_c	23.21	4.88

where ρ is the material density, V is the sample volume, and n_{ph} is the temperature-dependent phonon population factor. We evaluate $W^{OP}(\mathbf{k})$ taking into account both intravalley processes and intervalley L-L scattering events for which the initial and final electronic states belong to different degenerate L valleys. Furthermore, also intervalley L-Γ_c events have been considered. For each of these channels, we use the values of the effective phonon energy $\hbar\omega_{ph}$ and effective deformation potential D_{eff} reported in Table III according to the estimates of Ref. [63].

Since the interaction matrix element does not depend on the exchanged momentum, the sum over the final states for a given scattering channel can be calculated analytically, and one finds

$$W^{OP}(\mathbf{k}) = \left(n_{ph} + \frac{1}{2} \mp \frac{1}{2}\right)\frac{g D_{eff}^2}{4\pi\rho\omega_{ph}}\left(\frac{2m_{DOS}}{\hbar^2}\right)^{\frac{3}{2}} \times \frac{(\varepsilon_{\mathbf{k}} \pm \hbar\omega_{ph})^{1/2}}{1 + e^{(E_F \mp \hbar\omega_{ph} - \varepsilon_{\mathbf{k}})/k_B T}}\Theta(\varepsilon_{\mathbf{k}} \pm \hbar\omega_{ph}), \tag{11}$$

where m_{DOS} is the density-of-states mass associated to the final valley; for L electrons $m_{DOS} = (m_l m_t m_t)^{\frac{1}{3}}$ where $m_l = 1.792\, m_0$ and $m_t = 0.0984\, m_0$ are the longitudinal and transverse Ge conduction effective masses, respectively. In Eq. (11), g is the valley degeneracy of the final state and it is equal to one except for L-L intervalley scattering for which $g = 3$; $\Theta(\varepsilon_{\mathbf{k}} \pm \hbar\omega_{ph})$ is the Heaviside function ensuring energy conservation and for L-Γ scattering, its argument has to be substituted with $\varepsilon_{\mathbf{k}} - \Delta_{\Gamma L} \mp \hbar\omega_{ph}$, where $\Delta_{\Gamma L}$ is the Γ-L energy barrier (set to 149 and 141 meV at low T and room T, respectively [64,65]).

The scattering rate $S^{OP}(\varepsilon)$ per units of volume and excess electron energy (ε) is obtained from Eq. (11), summing over all the $\mathbf{k}$ states with energy between ε and $\varepsilon + d\varepsilon$ and over all the different scattering channels. This requires the trivial evaluation of the following expression:

$$S^{OP}(\varepsilon)d\varepsilon = \frac{1}{V}\sum_{\text{abs,em}}\sum_{\mathbf{k}}\sum_{\text{intra,inter}} W^{OP}(\mathbf{k})\delta(\varepsilon_{\mathbf{k}} - \varepsilon)d\varepsilon. \tag{12}$$

Charged impurities. Coulomb scattering by charged impurities is known to be the main cause of reduction of dc electron mobility in heavily doped semiconductors. This is due to the fact that the average distance among ionized donors at these high densities is much lower than the electron mean-free path observed in lightly doped or remotely doped materials, this latter quantity being much longer than the typical mean-free path of carriers in metals or oxides.

We calculate the charged-impurity scattering rate considering single center screened scattering in the Born approximation, following the Brooks-Herring approach (see, for instance,

Ref. [50]). To this aim, we use the experimentally determined values of N_A. It follows that the resulting T dependence of the scattering rate is to a certain extent mitigated by the fact that the number of ionized donors N_A is almost constant against temperature variations since at these high doping concentrations, the material is in the metallic regime. For what concerns the doping dependence, we notice that the scattering rate increases less than linearly with the number of scattering centers. This is due to the fact that increasing N_A the Coulomb interaction of each charged impurity is reduced by the larger free-carriers concentration which enhances the screening effect. The impurity scattering rate $W^{IM}(\mathbf{k},\mathbf{k}')$ for a carrier with initial electronic momentum $\mathbf{k}$ and final momentum $\mathbf{k}'$ is given by

$$W^{IM}(\mathbf{k},\mathbf{k}') = \frac{2\pi N_A}{V\hbar}\left(\frac{e^2}{\epsilon_0\epsilon_\infty}\right)^2 \frac{1}{\left[|\mathbf{k}-\mathbf{k}'|^2 + q_{TF}^2\right]^2} \times \delta(\varepsilon_{\mathbf{k}} - \varepsilon_{\mathbf{k}'})(1 - f_{\varepsilon_{\mathbf{k}'}}), \quad (13)$$

where V is the sample volume, ϵ_∞ is the Ge static dielectric constant, and q_{TF} is the Thomas-Fermi inverse screening length [50]. Since $W^{IM}(\mathbf{k},\mathbf{k}')$ rapidly decreases with the magnitude of the exchanged momentum, only L-L intravalley events have been taken into account. Due to the high dopant concentration, which is well above the density at which the Mott transition occurs, in our calculation we consider a temperature-independent dopant density N_A, setting as input value $N_A = n_{IR}$ (see Table I). Consequently, we assume that q_{TF} is mainly determined by the response of free electrons in the four equivalent L valleys, and neglect the contribution to the static screening length originating from bound carriers. With this assumption, q_{TF} is evaluated following Ref. [50], by numerical integration.

The total scattering rate $W^{IM}(\mathbf{k})$ is calculated integrating over the final states. To this aim, one has to consider the nonisotropic L-valley energy dispersion

$$\varepsilon_{\mathbf{k}} = \frac{\hbar k_x^2}{2m_l} + \frac{\hbar k_y^2}{2m_t} + \frac{\hbar k_z^2}{2m_t}. \quad (14)$$

We stress that, due to the nonspherical character of the L valleys, contributions to $W^{IM}(\mathbf{k})$ originating from a given valley depend not only on the $\mathbf{k}$ modulus, but also on its orientation with respect to the principal axes of the effective mass tensor in that valley. It follows that no analytical solution for the integral over the final state can be obtained and only a numerical evaluation of $W^{IM}(\mathbf{k})$ is viable. To this aim, we follow the approach outlined in Ref. [66] where a variable rescaling in $\mathbf{k}$ space for valley sphericization and the conservation of energy are exploited to obtain a double integral over the projection of the final-state momentum along the longitudinal direction and over the angle between the initial and final $\mathbf{k}$ vectors, projected in the parallel plane. $W^{IM}(\mathbf{k})$ is subsequently used to calculate the scattering rate $S^{IM}(\varepsilon)$ per units of volume and excess electron energy. This latter quantity is obtained summing over all the initial states with energy between ε and $\varepsilon + d\varepsilon$ as in Eq. (12) and considering the contributions of the fourfold degenerate L valleys.

Acoustic phonons. The interaction of electrons with acoustic phonons is expected to give a minor contribution to the total electron scattering rate, especially when the energy of one electron above E_F is high enough to emit an optical phonon, i.e., for $(\hbar\omega - E_F) \gtrsim 23$ meV. A simplified derivation of the acoustic phonon scattering rate (not shown), based on the deformation potential and the assumption of equipartition of electron energy, demonstrates that acoustic phonons do not have a significant influence on the overall tendency of the total scattering rates. Note that the effect of acoustic phonon scattering could be derived from a future detailed analysis of the T-dependent Hall effect data [44]. Looking at the experimental curves of Fig. 8, one can assign the deviation of $\gamma'(\omega)$ below 200 cm^{-1} from the almost-linear dependence on ω, more visible at room T, to the signature of acoustic phonon scattering.

Neutral impurities and crystal defects. Neutral impurities scatter electrons through static deformation of the periodic potential that shape the electronic band structure. Inactivated dopants are certainly present in our samples with densities N_I of the same order of magnitude of N_A. Nevertheless, their contribution to the scattering of carriers is certainly much smaller than the one caused by their charged counterpart since in the first case the interaction with carriers is far weaker [44]. Dislocations also contribute to electron scattering, but, looking at Fig. 8, the almost identical value of the experimental scattering rate for samples 9336 (grown on Ge wafer) and 9335 (grown on Si wafer with much higher dislocation density) indicates that the effect of dislocations can be safely neglected in our calculations.

Total scattering rate. As motivated by the above considerations, we evaluate the total scattering rate of electrons at the L points $S(\varepsilon) = S^{OP}(\varepsilon) + S^{IM}(\varepsilon)$ per unit of volume and excess electron energy considering only interactions with optical phonons and charged impurities. To this aim, literature values of the material parameters and experimentally determined ionized concentrations ($N_A = n_{IR} = n$) have been used. Notice also that the Fermi level E_F governing $S^{OP}(\varepsilon)$ and $S^{IM}(\varepsilon)$ has been self-consistently determined in each sample to reproduce the measured free-carrier density. Our numerical results are summarized in the top panels of Fig. 9.

The average electron scattering rates (in arbitrary units) as a function of the photon energy $\hbar\omega$ have been calculated as

$$\gamma_{theo}(\omega) = \frac{1}{n}\int_0^\infty \sqrt{\varepsilon}\, f_\varepsilon\, S(\varepsilon+\hbar\omega)\sqrt{\varepsilon+\hbar\omega} \times (1 - f_{\varepsilon+\hbar\omega})d\varepsilon, \quad (15)$$

where f_ε and $f_{\varepsilon+\hbar\omega}$ are the Fermi factors for the occupation probability of the electronic states with energy ε and $\varepsilon + \hbar\omega$, respectively, and $S(\varepsilon + \hbar\omega)$ is the total scattering rate in units of energy $(\varepsilon + \hbar\omega)$ and volume as from Eq. (12) of the paper. The occupation probability of the states at each T and for each value of the Fermi level (set by N_A) is calculated by the corresponding Fermi-Dirac distribution functions. Thus, the above expression for the total average scattering rate introduces further dependence on both doping and T with respect to the single-particle scattering cross sections. The calculation in Eq. (15) has been also performed separately for the optical phonon scattering S^{OP} and the charged-impurity scattering S^{IM}, hence allowing one for evaluating the relative importance of the two phenomena in Figs. 9(e)–9(h). It turns

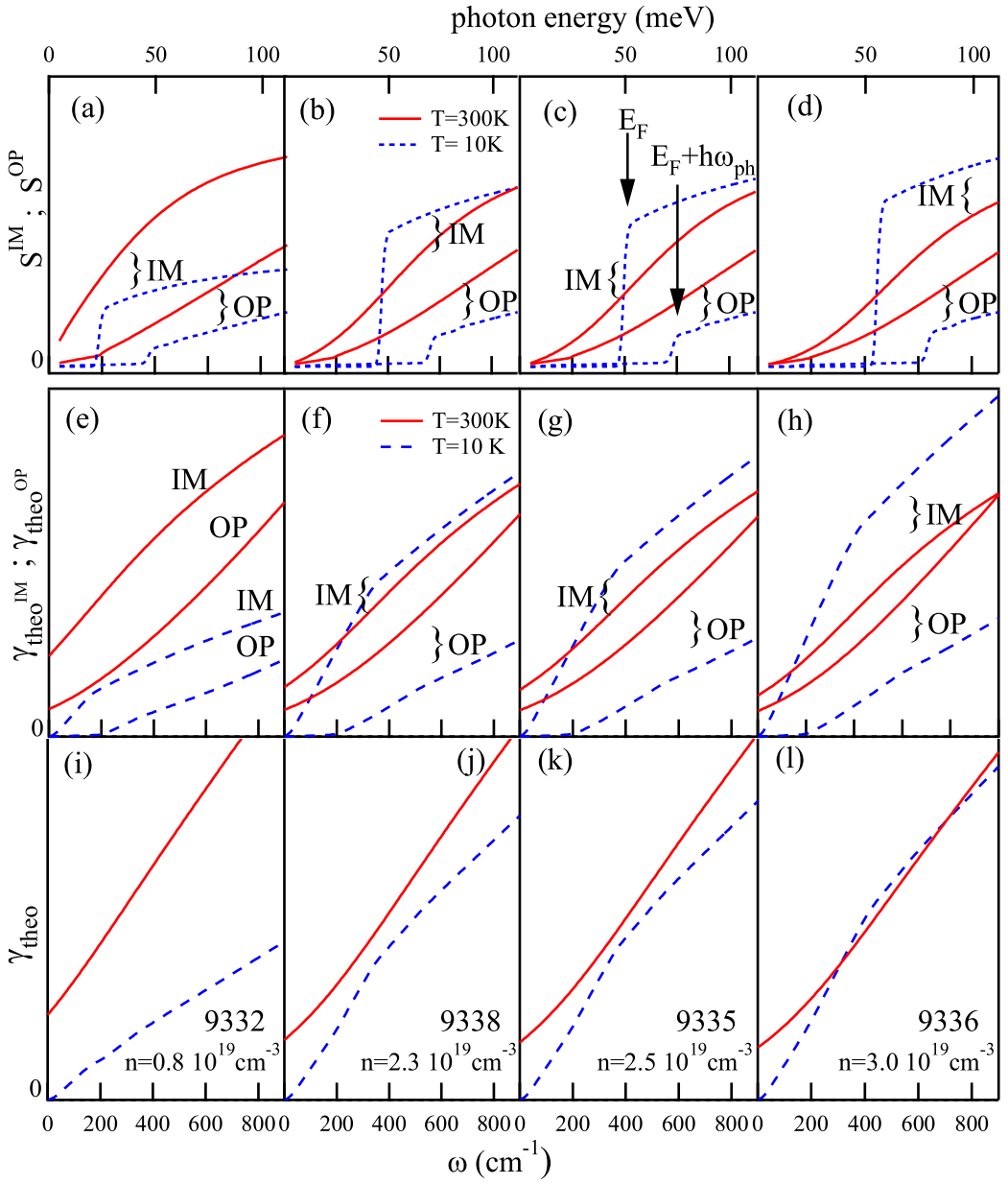

FIG. 9. The calculated excess-energy-dependent scattering cross sections per single electron (a)–(d) and the scattering rates averaged over all electrons (e)–(l) in the conduction band minima of n-Ge. The Fermi level E_F was chosen to give an electron density equal to the n_{IR} of samples of the 933× series. All calculations have been performed at $T = 10$ K (dashed blue lines) and 300 K (continuous red lines). In (a)–(d), the single-particle cross sections at 10 K display onsets at E_F and $E_F + \hbar\omega_{ph}$ for the two scattering mechanisms, respectively [see arrows in panel (c)]. In (e)–(h), the average contributions to losses from charged-impurity scattering (IM) and optical phonon scattering (OP) are plotted separately. In (i)–(l), it is shown the sum of the two scattering contributions in (e)–(h), which can be compared with the experimental data in Fig. 8.

out that, depending on IR frequency ω, temperature T, and free-electron density n, one or the other phenomenon may become dominant, but in general both effects have to be taken into account for a proper determination of plasmon losses in heavily doped Ge.

Finally, the overall tendency of the experimental curves $\gamma'(\omega)$ plotted in Fig. 8 is fully captured by the calculated $\gamma_{theo}(\omega)$ plotted in Figs. 9(i)–9(l): both experimental and theoretical scattering rates increase with frequency, are higher at room T than at low T in all samples, and slightly increase with doping at all T's. The zero-frequency value of $\gamma_{theo}(\omega)$ is higher at 300 K than at 10 K due to the larger optical phonon population, while the low-frequency extrapolation of $\gamma'(\omega)$ in Fig. 8 should be due to both acoustic and optical phonons. The different functional form of $\gamma'(\omega)$ in Fig. 8 and of $\gamma_{theo}(\omega)$ in Fig. 9 may be ascribed both to the approximation used in the theoretical calculations for the elastic scattering by charged impurities, which displays a sublinear dependence on ω, and to the propagation of systematic errors in the experimental data analysis procedure [KK and calculation of $\tilde{\gamma}(\omega)$].

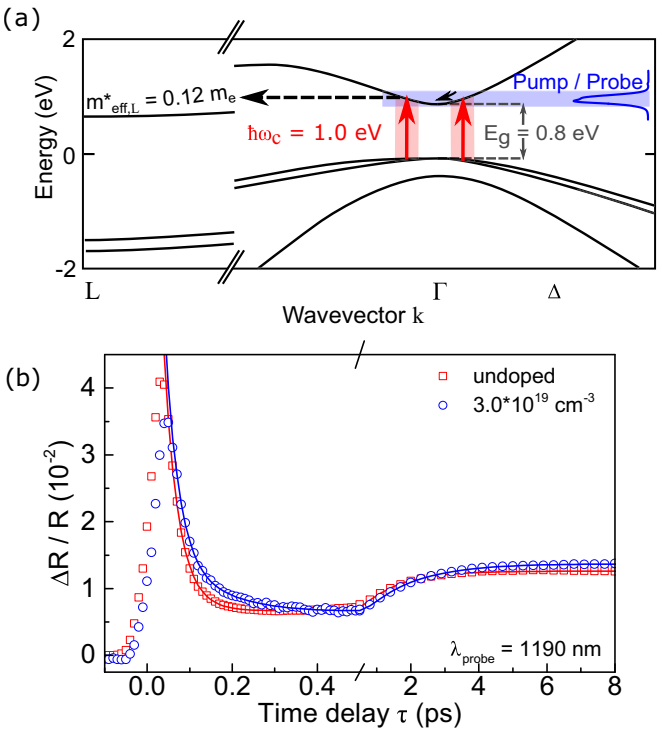

FIG. 10. (a) A simplified band structure of Ge depicting the impulsive excitation of electrons with a 20-fs pump pulse. $h\nu_c$ is the excitation photon energy and E_g the direct band gap. The arrows represent the scattering processes 1 and 2 occurring on a sub-ps time scale (see text): electron thermalization in Γ (solid arrow) and intervalley scattering (dashed arrow). (b) The transient reflectivity in the two samples as a function of time delay. Squares and circles depict the experimental data for the undoped and doped specimens, respectively. Solid lines are the results of the fitting with a triexponential function. Notice the change of scale in the horizontal axis.

IV. PUMP-PROBE SPECTROSCOPY

Time-resolved transient reflectivity measurements were conducted on two Ge films grown on silicon substrates: one identical to 9007 and one nominally undoped. The experimental setup employs an optical parametric amplifier driven by an Yb:KGW regenerative laser system. This source delivers 20-fs near-IR pulses with 50-kHz repetition rate and wavelength components between 1000 and 1400 nm. The experiments are conducted in a degenerate geometry and the beam is split in two replicas, one used for resonant excitation of electrons from valence to conduction band at the Γ point and one to probe the normal reflectivity change at a variable delay (see Fig. 10) [67]. The pump spectrum allows for the selective excitation of direct transition in Ge while leaving the Si substrate unperturbed [68]. The transient reflectivity is acquired by spectrally filtering the probe pulse at the wavelength 1190 nm with a monochromator equipped with an InGaAs photodiode. The detection is based on a lock-in scheme with mechanical modulation of the pump beam with a chopper wheel. The excitation fluence is kept at the moderate value of 500 μJ/cm^2 to minimize two-photon absorption that would directly create electron-hole pairs at the L point [69,70].

Figure 10(a) sketches the pump-probe experiments in Ge. The electronic distribution that follows the 20-fs pump pulse is centered at the direct gap where the electrons display excess energy thus being in a nonequilibrium state. The evolution of this perturbed system is determined by four main physical processes [71]: (i) thermalization in the Γ valley mainly via electron-electron scattering processes (this process is extremely fast and leads the electronic subsystem to a well-defined hot temperature); (ii) intervalley scattering of electrons to populate the L valleys; (iii) hot-electron cooling in the L valleys to reach an equilibrium with the lattice temperature; (iv) electron-hole recombination. The latter process occurs on a relatively long time scale in an indirect semiconductor as Ge and as such is not addressed by this study. The first three mechanisms are instead extremely interesting in the context of mid-IR plasmonics since they are related to the same fundamental interactions between electrons and lattice and between electrons and impurities that determine the plasmon losses.

Figure 10(b) shows the experimental traces of transient reflectivity as a function of time delay between pump and probe. The largest contribution to the signal occurs at early times for both samples. In fact, upon photoexcitation the semiconductor bleaches via Pauli blocking until the electrons are in the center of the Brillouin zone. Subsequently, the signal evolves via three time scales assigned to the first three processes discussed above: τ_1 is associated with the thermalization process within the Γ valley, τ_2 with the intervalley scattering, and τ_3 with the electron cooling in the L valley. Of course, one has $\tau_1 < \tau_2 < \tau_3$. Their value is retrieved by fitting a triexponential function to the experimental data. The values obtained for the two fast processes are nearly independent on doping [$\tau_1 \simeq 33$ fs for both samples and $\tau_2 \simeq 194$ (206) fs for the undoped (doped) sample]. It should be noted that these experimental values are due to the reflectivity change at one specific probe photon energy. Their value is only related to the characteristic scattering time of one specific class of processes. In fact, electron scattering contributes to the reflectivity change only after a number of events large enough to significantly change the electron distribution. Interestingly, the characteristic time τ_3, which is related to cooling within the L valley, differs significantly between the two samples. It is longer for the nominally undoped sample ($\tau_3 \simeq 1.4$ ps) than for the doped one ($\tau_3 \simeq 1.0$ ps), apparently due to the presence of charged impurities. In fact, the combination of processes (i) and (ii) results in a hot-electron population in the L valleys having an energy spread of few hundreds of meV. This hot-electron population relaxes to quasiequilibrium with the lattice by two distinct scattering mechanisms as described in the previous section: inelastic phonon scattering that directly releases energy to the lattice, and elastic charged-impurity scattering events that release no energy but rearrange the occupation of electronic states, making inelastic processes more probable. Also, the (cold) electrons already present in the L valleys of the doped sample impact on energy relaxation through Pauli blocking.

The energy relaxation mediated via scattering with phonons is of high interest here because it shares some features with the energy relaxation time of a collective plasmon excitation of energy $E_{\rm pl} \simeq k_{\rm B} T_{e,0}$ where $T_{e,0} \gg 300$ K is the electron

temperature in the L valley at time delay equal to τ_2. We can therefore define a plasmon-phonon energy relaxation time τ_{pl} and tentatively identify it with τ_3 of the nonintentionally doped sample. The energy lost by one electron in one single inelastic scattering event may be smaller than its total excess energy, and events resulting in electron energy increase (phonon absorption) can also occur. Therefore, many single-electron scattering events are needed for cooling the entire electron population and reach the equilibrium with the lattice, and we can expect τ_{pl} to be much larger than the average value of the electron scattering time $\langle[2\pi c\gamma(\omega)]^{-1}\rangle_\omega \sim 0.05$ ps. Indeed, we found $\tau_3 \sim 1.4$ ps $\gg 0.05$ ps, indicating that a number of single-electron scattering events $\gtrsim 30$ are needed for plasmon-phonon energy relaxation. In the doped sample, the increased energy relaxation efficiency due to the presence of charged impurities is consistent with a shorter $\tau_3 \sim 1.0$ ps, hence a shorter plasmon decay time.

The above speculation is useful to get rough estimates of mid-IR plasmon decay times and to understand the relation between τ_3 and τ_{pl}, but it does not allow us to conclude that τ_3 is a direct measure of this quantity. In fact, the evolution of the nonequilibrium electron distribution prepared by the pump pulse in zero external field is not the same process as the damping of plasmons excited by a continuous-wave radiation source. Although the energy spread of the electron distributions may be comparable in the two cases, they are certainly different in terms of the momentum distribution (see sketch in Fig. 1). Moreover, while in steady-state plasmon excitation $N_A \simeq n$, in the pump-probe experiment $N_A < n$ and a hole gas with density $p \simeq n$ is also present. For these reasons, the average electron scattering rates are expected to be higher in the pump-probe case, therefore, τ_3 may represent only a lower bound for the actual plasmon decay time. Nevertheless, it can be stated that the pump-probe data are consistent with the steady-state spectroscopy data, in the sense that there is no contradiction in assuming that the same single-electron scattering mechanisms govern plasmon decay and hot-electron relaxation after optical pumping. The n-Ge energy relaxation in the mid-IR range seems to be a much slower process than single-electron inelastic scattering and therefore at odds with group III-V semiconductors because of the lack of polar optical phonons, as already observed in n-Ge quantum-well systems [72].

V. DISCUSSION

We have observed that the increase of the electron mean-free path when cooling semiconductors (including Ge) at cryogenic temperatures, usually observed in dc transport, microwave, and terahertz spectroscopy experiments, has almost no counterpart in heavily doped n-Ge at mid-IR frequencies. We attributed this behavior to the peculiar frequency dependence of the electron-phonon and electron-charged-impurity scattering cross sections in n-Ge, and this interpretation can probably be extended to other heavily doped semiconductors with Fermi level close to the minimum of a parabolic band. This means that, with cooling, there is not much to be gained in terms of mid-IR plasmon losses in semiconductors. Also, this may explain why high-mobility semiconductors such as Ge or InAs did not provide significant advantages in terms of quality

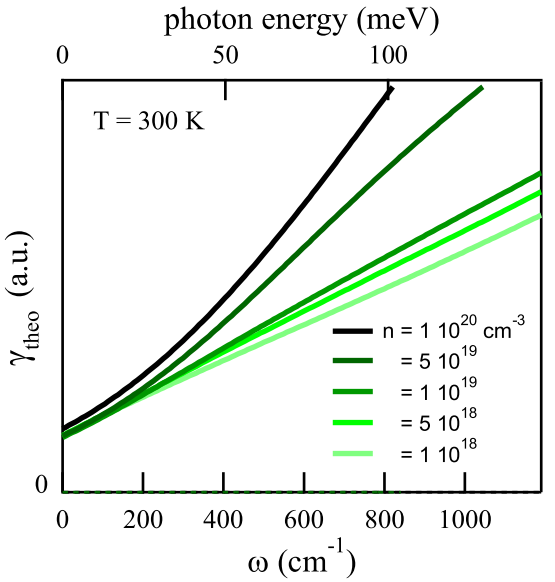

FIG. 11. Calculated average electron scattering rate in electron-doped Ge as a function of IR frequency for different values of the free-electron density. The data presented in this work up to $n \simeq 3\times10^{19}$ cm^{-3} confirm the model prediction.

factor of plasmonic resonances when employed for plasmonic sensing in the mid-IR [18,19]. The positive result of this study is that, by increasing the doping level from $n \simeq 1\times10^{18}$ to $\simeq 3\times10^{19}$ cm^{-3} as required for mid-IR plasmonics, the plasmon decay time does not decrease significantly because of the increased efficiency of free carriers in screening the charged-impurity scattering field for electrons oscillating at mid-IR frequencies. Figure 11, based on the model reported in this work, projects this trend up to 1×10^{20} cm^{-3} and the mild increase in the calculated scattering rate γ_{theo} is still not proportional to n. Also, the Brooks-Herring approach to impurity scattering calculation may not be fully valid for $n > 3\times10^{19}$ cm^{-3} [73]. Once again, this behavior is in contrast with the clear drop in the dc mobility with increasing doping. Therefore, the dc mobility cannot be used as a relevant parameter for losses in mid-IR plasmonics.

The experimental data presented in this paper also allows one to draw some conclusion on the relation between the average electron scattering time and the surface plasmon decay time. In the hydrodynamic regime, the electron-electron collisions conserve the total momentum and energy of the electron system. The hydrodynamic hypothesis corresponds to the assumption that all electrons at a given position contribute to the surface plasmon excitation. In this condition, the electron-electron collisions do not change the total electron momentum and energy, therefore, they do not affect the plasmon decay time. On the other hand, electron-phonon and electron-charged-impurity scattering events do not conserve the total momentum and/or energy and therefore they are certainly responsible for the plasmon decay. We have found, however, that a large number of single-electron scattering events are required for plasmon decay in n-Ge, as suggested by time-resolved data, and intrinsic decay times of few picoseconds may be expected for mid-IR plasmons in

nanostructures. The shorter $\tau_3 \sim 1.0$ ps found for the doped sample if compared to $\tau_3 \sim 1.4$ ps for the undoped one is probably due to the additional charged-impurity (elastic) scattering contribution that increases the efficiency of energy relaxation. A similar energy relaxation efficiency increase also leads to the doping-dependent increase of $\gamma(\omega)$ seen in Figs. 8–10. With a radiation period of 30 fs at $\omega \sim 1000$ cm^{-1} ($\lambda \simeq 10$ μm), one can therefore assume that, even in heavily doped samples at room T, several cycles of plasma oscillation will take place before complete energy damping.

It should be noted that the band-structure considerations made in the introduction are based on the corpus of experimental and theoretical knowledge acquired in many decades on the physical properties of bulk Ge crystals and do not necessarily hold for Ge thin films produced with all growth methods, substrate types, and thicknesses. The documented high-crystal quality of the Ge films grown by CVD studied in this work explains why, in the heavy-doping range of interest for plasmonic applications, the measured electron mobility of CVD films does not deviate significantly from what reported for single-crystal heavily doped samples [74,75], suggesting that scattering with dislocations has a negligible effect on charge transport. The mid-IR response of CVD films measured in this work is also virtually identical to that reported in the literature for bulk Ge crystals at comparable doping level [52], therefore, we find that crystal defects introduced by CVD growth are irrelevant as far as mid-IR optical properties are concerned.

One effect that is not discussed in this work is the impact of the **k**-space direction of electron scattering on the plasmon decay time. This topic is somehow related to the difference between the isotropic momentum relaxation of optical scattering events and the strong dependence of the dc electron mobility on the direction of the exchanged momentum (or scattering angle) in the scattering event. For example, scattering events that produce exchange of momentum in the direction transverse to the plasmon wave vector may impact on the plasmon decay time differently from scattering events changing the momentum parallel to the plasmon wave vector. Another effect to be addressed is the matching of both frequency and mode symmetry between plasmon and phonon oscillations (polaritonic effect), which may lead to faster resonant plasmon decay at specific frequencies and wave vectors. This resonance effect is well known for polar phonons in III-V semiconductors [76] and it has been recently studied in the case of the surface plasmons of the graphene/SiO_2 system finding a striking decrease of the plasmon lifetime above the SiO_2 phonon energy [77]. Also, given that the highest obtained $\hbar\omega^* \sim 0.15$ eV are well below the electron-hole pair-recombination energy threshold at $E_g = 0.66$ eV, we did not consider Landau damping as a possible decay path for plasmons [77]. Finally, acoustic phonon scattering has not been considered in our first-principles calculations and the density of states has been assumed to be perfectly parabolic.

Given the comparable contributions of electron-phonon and electron-charged-impurity scattering to plasmon decay, one could speculate that the electron-hole plasma in optically pumped intrinsic germanium [69] would display highly tunable n together with plasmon decay times dominated by electron-phonon scattering hence twice longer than those of plasmons in doped materials with comparable static electron (or hole) density. Intervalence band transitions, however, will be activated in an electron-hole plasma created by optical pumping: further studies are required in order to verify whether mid-IR plasmons in optically pumped intrinsic semiconductors display higher, comparable, or lower losses than those of plasmons in static heavily doped materials [70].

VI. CONCLUSIONS

In conclusion, we have investigated the electron scattering mechanisms in heavily n-doped germanium thin films grown on silicon wafers and intended for mid-IR plasmonics and metamaterial applications. Hall transport measurements and IR spectroscopy data interpreted within the Drude-Lorentz model are in good agreement with the estimate of the free-carrier density, that can reach 3×10^{19} cm^{-3}, which corresponds to a screened plasma frequency of $\sim$1200 cm^{-1} or a plasma wavelength of 8 μm. The plasmon decay times cannot be estimated by the dc mobility, nor within the Drude-Lorentz model, because of inconsistency between the single-valued Drude scattering rate and the actual frequency-dependent scattering rate. We determined the latter quantity both experimentally, by Kramers-Kronig transformations, and theoretically, by first-principles calculations. We have found a comparable role of electron-phonon and electron-charged-impurity scattering in n-Ge. The average electron scattering rate, in the range of 10 to 30 fs for heavily doped films, increases strongly with excitation frequency, weakly with temperature, and it is almost constant with doping. Interband pump-probe experiments on heavily doped n-Ge films suggest that the decay time of collective (plasmon) excitation may reach few picoseconds, allowing for underdamped mid-IR plasma oscillations even at room temperature.

Plasmonic devices based on heavily doped germanium films grown on silicon wafers could possibly be used for the integration of optoelectronic platforms in silicon microelectronic chips. Therein, plasmon-enhanced mid-infrared spectroscopy sensors may be combined with radiation sources and detectors, and the related acquisition electronics [1]. Gold, although often used to fabricate mid-infrared plasmonic nanostructures because it behaves as a very good conductor in this frequency range [3–7], is hardly compatible with the silicon-based complementary metal-oxide semiconductor transistor fabrication process, and its dielectric function is nontunable. In addition, genuine plasmonic effects such as the extreme field confinement provided by surface waves, epsilon-near-zero phenomena, or some metamaterial applications are not achievable with perfect conductors but rather require a truly plasmonic behavior [10–12], which can be roughly defined as the regime where the absolute value of the (negative) Re($\tilde{\epsilon}$) of the plasmonic material is of the order of the (positive) value of the dielectric constant of naturally occurring insulators, i.e., below $\sim$10. For gold in the mid-infrared, Re($\tilde{\epsilon}$) $\sim -10^3$, while for heavily doped germanium in the 500–900 cm^{-1} range, one has $-15 <$ Re($\tilde{\epsilon}$) < -1 as it can be seen in Fig. 7(b).

A final summary on the performance of heavily doped Ge for plasmonics can be given in terms of two recently introduced figures of merit (FOMs) [78], which describe the properties of surface plasmon polaritons (SPP) propagating

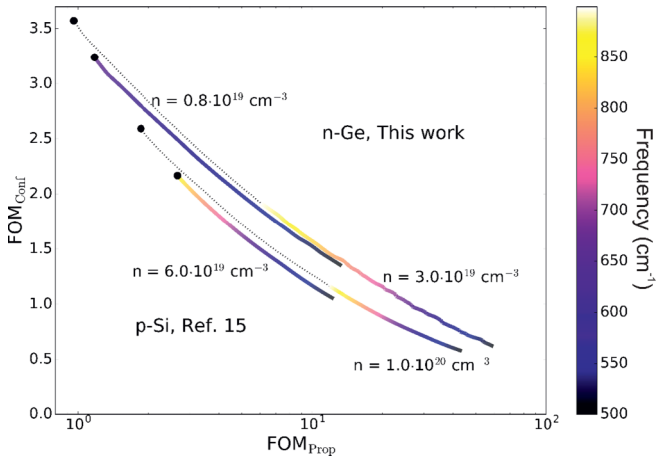

FIG. 12. The figures of merit for field confinement (vertical axis) and SPP propagation length (horizontal axis) for two n-type Ge samples presented in this work and two p-type Si samples presented in Ref. [15]. The color scale indicates the frequency at which the respective values are obtained. The dotted lines indicate the behavior above 900 cm^{-1}, up to the screened plasma frequency (black dot for each sample). Different materials achieve similar performances at different frequencies hence the impact of the tunability of the dielectric function on plasmonic designs.

at a metal-vacuum interface. The complex vector components $k_\parallel$ and $k_\perp$ (parallel and perpendicular to the metal surface, respectively) concur to determine the modulus of the SPP wave vector $k_{SPP} = \sqrt{k_\parallel^2 + k_\perp^2}$. The imaginary part of $k_\perp$ corresponds to the evanescent wave component and can be calculated from $\tilde{\epsilon}(\omega)$. Following Ref. [78], one can define a FOM for the characteristic SPP propagation length $FOM_{Prop} = k_{SPP}/2\pi \mathrm{Im}(k_\parallel)$, and a FOM for the field confinement towards the vacuum half-space as $FOM_{Conf} = \lambda/\mathrm{Im}(k_\perp)$. Figure 12 illustrates the result of such an analysis, performed in the 500–900 cm^{-1} range, which compares two Ge samples from this work (9332 and 9336) with the commercial heavily doped, p-type Si samples, whose dielectric function is reported in Ref. [15]. Silicon certainly represents a suitable alternative to germanium for group-IV mid-IR plasmonics. The analysis confirms that the n-type Ge material presented in this work compares favorably with Si in terms of FOM_{Prop} and FOM_{Conf}, briefly, because n-type Ge can reach a higher ω_p for a given free carrier and charged-impurity density.

Heavily doped Ge, although being characterized by significant losses as we thoroughly discussed throughout this work, seems to be a promising candidate to combine electromagnetic field confinement and integration with silicon microelectronics in future mid-infrared plasmonic chips. Perspectives for the possible use of heavily doped Ge in optoelectronic and biosensing chips are further reinforced by the already established use of undoped Ge for integrated mid-infrared waveguides [1]. Ongoing efforts to reach a higher carrier concentration on Ge thin films will improve the performances and extend the available palette of Ge materials for mid-infrared plasmonics.

ACKNOWLEDGMENTS

The research leading to these results has received funding from the European Unions Seventh Framework Programme under Grant Agreement No. 613055. The authors wish to thank G. Scappucci, M. De Seta, and M. Finazzi for stimulating discussions.

[1] R. Soref, Nat. Photon. **4**, 495 (2010).
[2] B. G. Lee, M. A. Belkin, R. Audet, J. MacArthur, L. Diehl, C. Pflügl, F. Capasso, D. C. Oakley, D. Chapman, A. Napoleone, D. Bour, S. Corzine, G. Hfler, and J. Faist, Appl. Phys. Lett. **91**, 231101 (2007).
[3] F. Neubrech, A. Pucci, T. W. Cornelius, S. Karim, A. Garcia-Etxarri, and J. Aizpurua, Phys. Rev. Lett. **101**, 157403 (2008).
[4] R. Adato, A. A. Yanik, J. J. Amsden, D. L. Kaplan, F. G. Omenetto, M. K. Hong, S. Erramilli, and H. Altug, Proc. Natl. Acad. Sci. USA **106**, 19227 (2009).
[5] R. L. Olmon, P. M. Krenz, A. C. Jones, G. D. Boreman, and M. B. Raschke, Opt. Express **16**, 20295 (2008).
[6] V. Giannini, Y. Francescato, H. Amrania, C. C. Phillips, and S. A. Maier, Nano Lett. **11**, 2835 (2011).
[7] C. DAndrea, J. Bochterle, A. Toma, C. Huck, F. Neubrech, E. Messina, B. Fazio, O. M. Marag, E. Di Fabrizio, M. Lamy de La Chapelle, P. G. Gucciardi, and A. Pucci, ACS Nano **7**, 3522 (2013).
[8] F. Yi, H. Zhu, J. C. Reed, and E. Cubukcu, Nano Lett. **13**, 1638 (2013).
[9] S. A. Maier, M. L. Brongersma, P. G. Kik, S. Meltzer, A. A. G. Requicha, and H. A. Atwater, Adv. Mater. **13**, 1501 (2001).
[10] J. B. Pendry, Phys. Rev. Lett. **85**, 3966 (2000).
[11] A. Boltasseva, Science **331**, 290 (2011).
[12] G. V. Naik, V. M. Shalaev, and A. Boltasseva, Adv. Mater. **25**, 3264 (2013).
[13] A. J. Hoffman, L. Alekseyev, S. S. Howard, K. J. Franz, D. Wasserman, V. A. Podolskiy, E. E. Narimanov, D. L. Sivco, and C. Gmachl, Nat. Mater. **6**, 946 (2007).
[14] J. C. Ginn, R. L. Jarecki, E. A. Shaner, and P. S. Davids, J. Appl. Phys. **110**, 043110 (2011).
[15] M. Shahzad, G. Medhi, R. E. Peale, W. R. Buchwald, J. W. Cleary, R. Soref, G. D. Boreman, and O. Edwards, J. Appl. Phys. **110**, 123105 (2011).
[16] D. Li and C. Z. Ning, Opt. Express **19**, 14594 (2011).
[17] S. Law, D. C. Adams, A. M. Taylor, and D. Wasserman, Opt. Express **20**, 12155 (2011).
[18] S. Law, L. Yu, A. Rosenberg, and D. Wasserman, Nano Lett. **13**, 4569 (2013).
[19] L. Baldassarre, E. Sakat, J. Frigerio, A. Samarelli, K. Gallacher, E. Calandrini, G. Isella, D. J. Paul, M. Ortolani, and P. Biagioni, Nano Lett. **15**, 7225 (2015).
[20] T. Minami, Semicond. Sci. Technol. **20**, S35 (2005).
[21] A. Berrier, R. Ulbricht, M. Bonn, and J. G. Rivas, Opt. Express **18**, 23226 (2010).
[22] M. Wagner, A. S. McLeod, S. J. Maddox, Z. Fei, M. Liu, R. D. Averitt, M. M. Fogler, S. R. Bank, F. Keilmann, and D. N. Basov, Nano Lett. **14**, 4529 (2014).

[23] C. Kurter, P. Tassin, L. Zhang, T. Koschny, A. P. Zhuravel, A. V. Ustinov, S. M. Anlage, and C. M. Soukoulis, Phys. Rev. Lett. **107**, 043901 (2011).

[24] C. Kurter, J. Abrahams, G. Shvets, and S. M. Anlage, Phys. Rev. B **88**, 180510(R) (2013).

[25] O. Limaj, F. Giorgianni, A. Di Gaspare, V. Giliberti, G. de Marzi, P. Roy, M. Ortolani, X. Xi, D. Cunnane, and S. Lupi, ACS Photon. **1**, 570 (2014).

[26] R. Hillenbrand, T. Taubner, and F. Keilmann, Nature (London) **418**, 159 (2002).

[27] J. D. Caldwell, A. V. Kretinin, Y. Chen, V. Giannini, M. M. Fogler, Y. Francescato, C. T. Ellis, J. G. Tischler, C. R. Woods, A. J. Giles, M. Hong, K. Watanabe, T. Taniguchi, S. A. Maier, and K. S. Novoselov, Nat. Commun. **5**, 5221 (2014).

[28] Y. Chen, Y. Francescato, J. D. Caldwell, V. Giannini, T. W. W. Mass, O. J. Glembocki, F. J. Bezares, T. Taubner, R. Kasica, M. Hong, and S. A. Maier, ACS Photon. **1**, 718 (2014).

[29] S. M. Sze and K. K. Ng, *Physics of Semiconductor Devices* (Wiley, Hoboken, New Jersey, 2007).

[30] B. W. Levinger and D. R. Frankel, J. Phys. Chem. Solids **20**, 281 (1961).

[31] O. Madelung, M. Schultz, and H. Weiss, *Semiconductor Physics: Group IV Elements and III-V Compounds* (Springer, Berlin, 1982).

[32] J. Vanhellemont and E. Simoen, Mater. Sci. Semicond. Proc. **15**, 642 (2012).

[33] G. Scappucci, W. M. Klesse, L. A. Yeoh, D. J. Carter, O. Warschkow, N. A. Marks, D. L. Jaeger, G. Capellini, M. Y. Simmons, and A. R. Hamilton, Sci. Rep. **5**, 12948 (2015).

[34] K. Takinai and K. Wada, J. Appl. Phys. **119**, 181504 (2016).

[35] D. Chrastina, G. Isella, M. Bollani, B. Rssner, E. Mller, T. Hackbarth, E. Wintersberger, Z. Zhong, J. Stangl, and H. Von Knel, J. Cryst. Growth **281**, 281 (2005).

[36] R. Geiger, J. Frigerio, M. J. Süess, D. Chrastina, G. Isella, R. Spolenak, J. Faist, and H. Sigg, Appl. Phys. Lett. **104**, 062106 (2014).

[37] C. Rosenblad, H. R. Deller, T. Graf, and E. Muller, J. Cryst. Growth **188**, 125 (1998).

[38] J. Osmond, G. Isella, D. Chrastina, R. Kaufmann, M. Acciarri, and H. Von Känel, Appl. Phys. Lett. **94**, 201106 (2009).

[39] K. Gallacher, P. Velha, D. J. Paul, I. MacLaren, M. Myronov, and D. R. Leadley, Appl. Phys. Lett. **100**, 022113 (2012).

[40] P. P. Edwards and M. J. Sienko, Phys. Rev. B **17**, 2575 (1978).

[41] M. N. Alexander and D. F. Holcomb, Rev. Mod. Phys. **40**, 815 (1968).

[42] G. A. Thomas, M. Capizzi, F. DeRosa, R. N. Bhatt, and T. M. Rice, Phys. Rev. B **23**, 5472 (1981).

[43] V. M. Babich, P. I. Baranskii, I. V. Dakhovskii, and A. G. Samoylovich, Ukr. Fiz. Zh. **14**, 418 (1969) [Phys. Stat. Sol. **33**, 879 (1969)].

[44] M. M. Mirza, D. A. Maclaren, A. Samarelli, B. M. Holmes, H. Zhou, S. Thoms, D. Macintyre, and D. J. Paul, Nano Lett. **14**, 6056 (2014).

[45] D. J. Paul, Laser Photon. Rev. **4**, 610 (2010).

[46] M. Dressel and G. Grüner, *Electrodynamics of Solids: Optical Properties of Electrons in Matter* (Cambridge University Press, Cambridge, UK, 2002).

[47] C. Xu, C. L. Senaratne, J. Kouvetakis, and J. Menndez, Appl. Phys. Lett. **105**, 232103 (2014).

[48] T. M. Donovan, W. E. Spicer, J. M. Bennett, and E. J. Ashley, Phys. Rev. B **2**, 397 (1970).

[49] M. Ortolani, P. Calvani, and S. Lupi, Phys. Rev. Lett. **94**, 067002 (2005).

[50] B. K. Ridley, *Quantum Processes in Semiconductors* (Oxford University Press, Oxford, UK, 2014).

[51] W. G. Spitzer and H. Y. Fan, Phys. Rev. **106**, 882 (1957).

[52] H. Y. Fan, W. Spitzer, and R. J. Collins, Phys. Rev. **101**, 566 (1956).

[53] L. Baldassarre, E. Calandrini, A. Samarelli, K. Gallacher, D. J. Paul, J. Frigerio, G. Isella, E. Sakat, M. Finazzi, P. Biagioni, and M. Ortolani, *2014 39th International Conference on Infrared Millimeter and Terahertz Waves (IRMMW-THz)* (IEEE, Piscataway, NJ, 2014).

[54] J. W. Allen and J. C. Mikkelsen, Phys. Rev. B **15**, 2952 (1977).

[55] W. Götze, Philos. Mag., Part B **43**, 219 (1981).

[56] P. B. Allen, Phys. Rev. B **3**, 305 (1971).

[57] S. V. Shulga, O. V. Dolgov, and E. G. Maksimov, Phys. C (Amsterdam) **178**, 266 (1991).

[58] J. W. van der Eb, A. B. Kuzmenko, and D. van der Marel, Phys. Rev. Lett. **86**, 3407 (2001).

[59] D. N. Basov and T. Timusk, Rev. Mod. Phys. **77**, 721 (2005).

[60] L. Degiorgi, Rev. Mod. Phys. **71**, 687 (1999).

[61] A. V. Puchkov, D. N. Basov, and T. Timusk, J. Phys.: Condens. Matter **8**, 10049 (1996).

[62] C. Jacoboni and L. Reggiani, Rev. Mod. Phys. **55**, 645 (1983).

[63] M. V. Fischetti and S. E. Laux, IEEE Trans. Electron. Device **38**, 650 (1991).

[64] Y. P. Varshni, Physica, **34**, 149 (1967).

[65] C. D. Thurmond, J. Electrochem. Soc. **122**, 1133 (1975).

[66] J. B. Krieger, T. Meeks, and E. Esposito, Phys. Rev. B **3**, 1262 (1971).

[67] X. Q. Zhou, H. M. van Driel, and G. Mak, Phys. Rev. B **50**, 5226 (1994).

[68] M. I. Gallant and H. M. van Driel, Phys. Rev. B **26**, 2133 (1982).

[69] B. Mayer, C. Schmidt, J. Bhler, D. V Seletskiy, D. Brida, A. Pashkin, and A. Leitenstorfer, New J. Phys. **16**, 063033 (2014).

[70] M. P. Fischer, Ch. Schmidt, E. Sakat, J. Stock, A. Samarelli, J. Frigerio, M. Ortolani, D. J. Paul, G. Isella, A. Leitenstorfer, P. Biagioni, and D. Brida, Phys. Rev. Lett. **117**, 047401 (2016).

[71] G. Mak and W. W. Rühle, Phys. Rev. B **52**, R11584(R) (1995).

[72] M. Ortolani, D. Stehr, M. Wagner, M. Helm, G. Pizzi, M. Virgilio, G. Grosso, G. Capellini, and M. De Seta, Appl. Phys. Lett. **99**, 201101 (2011).

[73] G. D. Mahan, J. Appl. Phys. **51**, 2634 (1980).

[74] V. I. Fistul, M. I. Iglitsyn, and E. M. Omelyanovskii, Sov. Phys.–Solid State **4**, 784 (1962).

[75] C. Hilsum, Electron. Lett. **10**, 259 (1974).

[76] G. C. Cho, T. Dekorsy, H. J. Bakker, R. Hövel, and H. Kurz, Phys. Rev. Lett. **77**, 4062 (1996).

[77] H. Yan, T. Low, W. Zhu, Y. Wu, M. Freitag, X. Li, F. Guinea, P. Avouris, and F. Xia, Nat. Photon. **7**, 394 (2013).

[78] B. Dastmalchi, Ph. Tassin, Th. Koschny, and C. M. Soukoulis, Adv. Opt. Mater. **4**, 177 (2016).